POLITECNICO DI TORINO

Collegio di Ingegneria Chimica e dei Materiali

Master of Science Course

in Materials Engineering for Industry 4.0

Master of Science Thesis

Prototyping and Characterization of Auxetic Materials for Space Applications



Tutor

Prof. Enrico Zappino

Candidate

Baran Sahin

Settembre 2026

ABSTRACT

This study investigates the prototyping and mechanical characterization of bistable auxetic materials designed for space applications. In this study, a multi-material Fused Deposition Modeling (FDM) 3D printing approach was used for the prototyping of rotating rigid square geometries; Tough PLA was chosen for the main frame and rigid squares, and TPU 95A was selected for the flexible hinges allowing rotational movement. A parametric study was performed and uniaxial tensile tests were conducted to evaluate the mechanical response of the designed multicellular systems. Mechanical test results demonstrated that hinge thickness, cell angle, and size of matrix cell are decisive in determining the macroscopic mechanical response. It has been observed that the most promising configuration directly depends on the requirements of the intended space mission. The findings reveal the great potential of auxetic materials with optimized geometric parameters for next-generation deployable space structures.

Table of Contents

1. Introduction and Literature Review 1
   1.1. Deployable Space Structures 2
      1.1.1. Rigid Deployable Space Structures 2
      1.1.2. Deformable Deployable Space Structures 4
      1.1.3. Inflatable Deployable Structures 4
   1.2. Auxetic Materials 5
   1.3. Geometric Classification of Auxetic Materials 7
      1.3.1. Re-entrant Structures 7
      1.3.2. Chiral Structures 8
      1.3.3. Rotating Rigid Units 8
      1.3.4. Origami Structures 9
   1.4. Considerations on the Choice of Geometry 9
   1.5. Bistable Mechanism in Auxetic Materials 10
   1.6. Fabrication Techniques of Auxetic Materials 12
      1.6.1. Additive Manufacturing 12
      1.6.2. Laser Cutting 13
      1.6.3. Auxetic Foam Fabrication 14
2. Design of Auxetic Structures 15
3. Materials, Manufacturing and Prototyping 19
   3.1. Selection of Manufacturing Method 19
   3.2. Multi-Material Requirement 19
   3.3. Process Parameters and Challenges 19
4. Mechanical Characterization and Testing 23
   4.1. Mechanical Testing Setup 23
   4.2. Testing Results 24
      4.2.1. 2 x 2 Specimens with Different Hinge Thicknesses 24
      4.2.2. 2 x 2 Specimens with Different Cell Angle 31
      4.2.3. 4 x 4 Specimens with Different Hinge Thicknesses 37
   4.3. Considerations on Geometric Parameters and Cell Sizes 44
      4.3.1. The Effect of Hinge Thickness 44
      4.3.2. The Effect of Cell Angle 44
      4.3.3. The Effect of Matrix Size 45
5. Conclusions and Future Developments 47
6. References 49

List of Figures

Figure 1. Telescopic Tubular Mast (TTM) developed by Astro Aerospace, from [6] 3
Figure 2. Antenna reflector designed by the European Space Agency (ESA), from [9] 3
Figure 3. A robot design with a tensegrity architecture, from [11] 4
Figure 4. The TRAC-boom structure, from [14] 4
Figure 5. Expansion progress of Bigelow Expandable Activity Module (BEAM), from [17] . 5
Figure 6. Axial tension material deformation. (A) Material with a positive Poisson ratio. (B) Material with a negative Poisson ratio, from [20]. 6
Figure 7. Re-entrant polymer foam with negative Poisson's ratio, from [23]. 6
Figure 8. Re-entrant honeycomb structure and the unit cell, from [31] 7
Figure 9. Axial tension deformation difference, from [32]. 8
Figure 10. Tetra-chiral structure, from [34]. 8
Figure 11. Rotating rigid squares structure expanding in both axes under tensile stress, from [36]. 9
Figure 12. Bistable and monostable energy landscapes, from [44]. 10
Figure 13. Bistable auxetic structures inspired by ancient motifs, from [48]. 11
Figure 14. Schematic of the FDM/FFF process, from [53] 13
Figure 15. Designed square block model 15
Figure 16. Flexible hinge design 16
Figure 17. Design of the single square unit cell 16
Figure 18. 2x2 matrix cell consisting of 4 square cells 17
Figure 19. 4x4 matrix cell consisting of 16 square cells 18
Figure 20. Rigid end tab design for axial tensile test 18
Figure 21. Bambu Lab A1 Mini 3D Printer 19
Figure 22. Negative dimensional offset operation applied to hinge design 21
Figure 23. The physical prototype of the multi-cell structure 21
Figure 24. The physical prototype of the multi-cell structure in the fully deployed state 22
Figure 25. Uniaxial tensile testing experimental setup for 4x4 matrix design. 23
Figure 26. Deployed structure of the multi-cell prototype after tensile testing. 24
Figure 27. The initial configuration of the 2x2 multi-cell specimen mounted in the universal testing machine. 25
Figure 28. Force-displacement curves of 2x2 specimens. 26
Figure 29. Enlarged view of the force-displacement curves in the initial displacement region (0-14 mm) for 2x2 specimens with varying hinge thicknesses. 27
Figure 30. Instantaneous stiffness (dF/dx) profiles as a function of displacement for 2×2 multi-cell matrices with varying hinge thicknesses (0.8 mm, 1.2 mm, and 1.6 mm). 28
Figure 31. The intermediate rotational phase of the 2x2 specimen during uniaxial tension. .. 29
Figure 32. Enlarged view of the force-displacement curves in the final deployment region (19-35 mm) for 2x2 specimens with varying hinge thicknesses. 30
Figure 33. The fully deployed and geometrically locked configuration of the 2x2 specimen. 31
Figure 34. The appearance of samples with different cell angles: (a) 10°, (b) 15°, (c) 20° and (d) 25° 32
Figure 35. Tensile test results comparing the force-displacement behaviour of 2x2 multicell matrix structures configured with cell angles of 10°, 15°, 20°, and 25°. 33
Figure 36. Enlarged view of the initial force-displacement response for 2x2 multi-cell structures with cell angles of 10°, 15°, 20°, and 25° 34

Figure 37. Instantaneous stiffness (dF/dx) profiles as a function of displacement for 2×2 multi-cell matrices with varying cell angles (10°, 15°, 20° and, 25°). 35
Figure 38. Enlarged view of the force-displacement curves in the final deployment region (22-36 mm) for 2x2 specimens with varying cell angles. 36
Figure 39. The initial configuration of the 4x4 multi-cell specimen mounted in the universal testing machine. 38
Figure 40. Force-displacement curves of 4x4 specimens 38
Figure 41. Enlarged view of the force-displacement curves in the initial displacement region (0-13 mm) for 4x4 specimens with varying hinge thicknesses. 39
Figure 42. Force-displacement curves of the 4x4 matrix in the 0–40 mm displacement range for specimens with varying hinge thicknesses. 40
Figure 43. Visual sequence of the 4x4 matrix during tensile testing: (a) initial local opening at the top row, (b) progressive downward deformation of the middle rows, and (c) the fully deployed and structurally locked configuration. 41
Figure 44. Instantaneous stiffness (dF/dx) profiles as a function of displacement for 4x4 multi-cell matrices with varying hinge thicknesses (0.8 mm, 1.2 mm, and 1.6 mm) 42
Figure 45. Enlarged view of the force-displacement curves in the final deployment region (45-70 mm) for 4x4 specimens with varying hinge thicknesses. 43

List of Tables

Table 1. FDM process parameters 20
Table 2. Parametric combinations of specimen cell sizes and hinge thicknesses 20
Table 3. Parametric combinations of specimen cell sizes and cell angles. 20
Table 4. Summary of key mechanical properties for 2x2 specimens with varying hinge thicknesses. 31
Table 5. Summary of key mechanical properties for 2x2 specimens with varying cell angles. 37
Table 6. Summary of key mechanical properties for 4x4 specimens with varying hinge thicknesses. 44

1. Introduction and Literature Review

One of the biggest obstacles in modern space applications is the necessity to overcome the strict physical limitations imposed by launch vehicles. High launch costs and aerodynamic constraints make the volume inside rocket fairings and the mass that can be carried into orbit a highly valuable resource. Systems requiring large surface areas, such as advanced space telescopes or habitat modules, must fit into the limited space of the rocket during launch and must simultaneously be designed at the ideal dimensions desired for the space mission. This situation forces designers into a challenging engineering compromise between mission objectives and physical constraints. Striking a balance between the two is highly critical.

The primary solution to overcoming volume constraints has been the use of deployable, expandable, and inflatable structures deployed in orbit. These structures are adaptable systems that can be transformed from packed launch configurations into an operational state during the mission. However, these systems have a mechanical architecture consisting of hinges, springs, locks, and motor mechanisms. These traditional systems are vulnerable to failure and possess serious flaws that could cause the entire mission to fail, as they are exposed to high acoustic and vibrational stresses during launch. Since it is practically impossible to physically repair these mechanical failures in the space environment, a need has arisen for lighter and more reliable alternatives that minimize the number of moving parts.

To overcome these challenges, current scientific research has focused on developing new-generation structural materials with superior performance that can replace traditional mechanisms. Metamaterials, which draw their strength from artificially designed micro/macro internal geometries rather than the chemical properties of the material, hold great importance in this field. In particular, mechanical metamaterials with a negative Poisson's ratio, known as auxetics, are attracting significant interest in this context. Auxetics expand transversely when subjected to tension and compress when subjected to compression. Their negative Poisson's ratios offer unique and versatile advantages for space applications. Specifically, their bistable variants will bring the added advantage of maintaining a folded state during launch without the use of a pre-loading system. Thanks to this advantage provided by the bistable structure, the number of moving parts and energy consumption in the deployable structure can be minimized while the reliability of both the structure and the space application is increased.

Although the theoretical advantages of auxetic materials in the aerospace industry are highly attractive, the design, manufacturing, and experimental validation of these structures' mechanical responses to space conditions remains an emerging field in the literature.

The main purpose of this study is to prototype bistable auxetic materials using a 3D printer and to perform their detailed mechanical characterization in order to investigate their potential in space applications. Within the scope of this study, the main types of auxetics will first be analyzed before focusing on bistable geometries. Then, bistable auxetic cell topologies with a rotating rigid unit structure, designed using the CAD program Altair Inspire, will be prototyped from TPU 95A and Tough PLA polymer materials using FDM/FFF printing technologies and examined through mechanical tests. Following this, the effect of varying geometric parameters, such as hinge thickness and cell angle, on cell performance will be analyzed and a parametric study will be conducted. Based on these results, different geometric designs will yield different outcomes according to the requirements of space applications. The experimental and analytical

findings obtained will demonstrate the importance of these innovative materials in future space missions.

1.1. Deployable Space Structures

Optimizing payload volume within a launch vehicle remains one of the challenges in space mission design [1]. Large-scale satellites and space habitats often exhaust the maximum capacity of heavy launchers. When structures exceed these limits, they must be engineered as modular segments and assembled in orbit. This approach is complex and costly, requiring multiple launches just to achieve a baseline level of operability [1].

Space constraints are equally critical for smaller structures. Since purchasing a dedicated launch is expensive for small missions, operators typically rely on rideshare configurations to distribute costs. While economical, this requires adhering to the dimensional limits of shared payload dispensers. Volume constraints often clash with the satellite's operational needs.

The development of deployable structures has become indispensable across the aerospace industry. To be successful, these structures must meet some requirements, such as [2], [3]:

- Occupy minimal volume when stowed and endure the mechanical loads of the launch phase.

- Transition into their final configuration, with the lowest possible risk of mechanical failure.

- Withstand the harsh conditions of the space environment throughout the mission's required operational lifespan once fully deployed.

Deployable space structures, based on their mechanisms and architectures, they can be divided into three main categories: rigid, deformable, and inflatable deployable structures.

1.1.1. Rigid Deployable Space Structures

Rigid deployable space structures are formed by assembling components that are non-deformable, in a manner that supports multi-dimensional mechanical movements. The relative motion of rigid components is achieved through hinges or cables connecting them. Subsequently, a stable form is attained by balancing the forces acting on the system. Deployment is typically achieved through the integration of systems such as motors or springs.

Thanks to their rigid structures, the shape of the deployed system is precisely controlled. However, the rigid connection points of these structures are highly susceptible to failure and can lead to system deviations [3]. Furthermore, the assembly of these structures may be disadvantageous in terms of cost. [4].

Telescopic structures are included in this category; these structures consist of coaxial circular tubes of varying diameters. [5]. When the telescopic structure is sent to its operational orbit, a motor within the assembly utilizes thrust to extend the structure. Figure 1 shows the Telescopic Tubular Mast (TTM) developed by Astro Aerospace in its deployed state.



Figure 1. *Telescopic Tubular Mast (TTM) developed by Astro Aerospace, from [6]*

Rigid deployable structures with a pantographic (scissor-like) configuration are quite common. Their primary characteristic is the presence of hinges resembling the shape of scissors. [7]. These structures are particularly useful in tasks where compactness and space efficiency are increasingly important [8]. These structures are widely used in space antennas that require high precision during the deployment phase. Figure 2 shows an antenna reflector designed by the European Space Agency (ESA) that features a double-pantograph deployable ring design.



Figure 2. *Antenna reflector designed by the European Space Agency (ESA), from [9]*

Another type of rigid deployable structure is the tensegrity structure. These structures incorporate both flexible members, such as cables, and rigid members, such as bars. While flexible members cannot carry significant loads other than tensile loads, rigid members bear loads of all types; this distinction allows the two types of members to be differentiated from one another [10]. These structures are of great importance for space applications due to advantages such as the simplicity of their components and their lightweight nature. However, the fact that the structure incorporates both rigid and flexible members complicates the balancing of internal forces. [8]. Figure 3 shows a robot design with a tensegrity architecture.



***Figure 3**. A robot design with a tensegrity architecture, from [11]*

1.1.2. Deformable Deployable Space Structures

Unlike rigid deployable structures, deformable deployable structures utilize the elastic deformation of materials. By applying a preload prior to launch, the structure's geometry is deformed to fit within the required volume. Once in space, the structure is deployed using methods such as motors, screw-nut couplings, or the release of stored elastic energy.

Coilable masts and Triangular Rollable and Collapsible (TRAC) structures serve as examples of such structures used in the aerospace field. Coilable masts consist of structures capable of folding onto themselves, and they deploy through the release of elastic energy [12]. TRAC booms, on the other hand, are popular in the small satellite sector due to their high packaging capacity [13]. The TRAC-boom structure is shown in Figure 4.

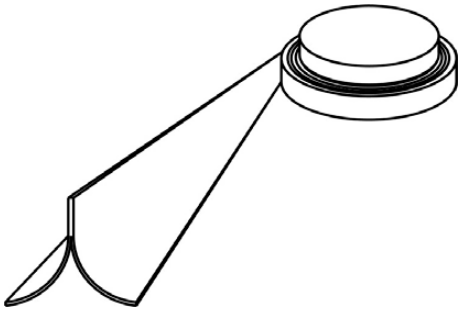


***Figure 4.** The TRAC-boom structure, from [14]*

1.1.3. Inflatable Deployable Structures

Inflatable deployable structures are designed for missions where deployment precision can be tolerated but a high packaging ratio is required. The system's deployment dynamics rely on the expansion of the film as it inflates from a compressed, packed state. This easily deployable film, which lacks inherent rigidity, constitutes the bulk of the structure's weight. Consequently, the system gains significant advantages such as low weight, minimal storage volume, structural simplicity, and low cost. [15]. However, there are certain disadvantages. Plastic deformations in the structure can damage gas circulation and forming precision. Additionally, micrometeoroids and orbital debris can puncture the structure, compromising its structural rigidity. [16]. Large inflatable antennas and modules can be cited as examples of such structures. Figure 5 illustrates the expansion progress of Bigelow Expandable Activity Module (BEAM).

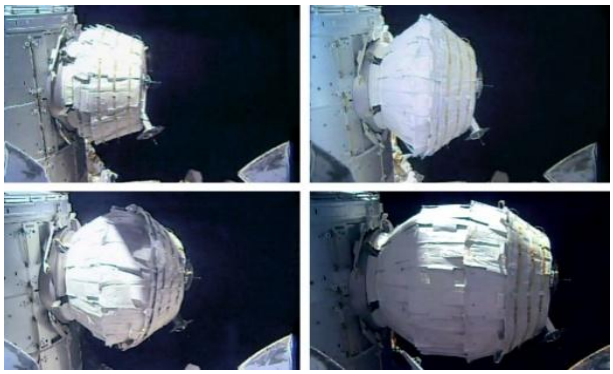


Figure 5. *Expansion progress of Bigelow Expandable Activity Module (BEAM), from [17]*

1.2. Auxetic Materials

Metamaterials are materials designed to provide properties not readily found in nature, and these properties are derived not from their chemical composition, but from their specially designed geometric micro and macro structures [18]. The resulting broad design freedom has therefore aroused considerable interest in many sectors of engineering, especially in the aerospace industry.

In materials science, a negative ratio of a material's transverse strain to its axial strain is defined as Poisson's ratio. Most of the conventional materials exhibit a positive Poisson's ratio due to the principles of mass conservation and thermodynamics [19]. However, auxetic materials, a class of mechanical metamaterials, exhibit the opposite behaviour. The reason behind this unusual negative Poisson's ratio property stems not from the material's chemical composition, but from its intrinsic geometric structure and cellular topology. This behaviour is achieved through specific deformation of the micro-scale structural cells of auxetic materials. Thanks to this specially designed intrinsic geometric structure, auxetic materials exhibit rotational or folding movements at the microscopic level under macroscopic loads, creating a simultaneous expansion or contraction behaviour throughout the material. Figure 6 shows the deformation of materials with positive and negative Poisson's ratios.

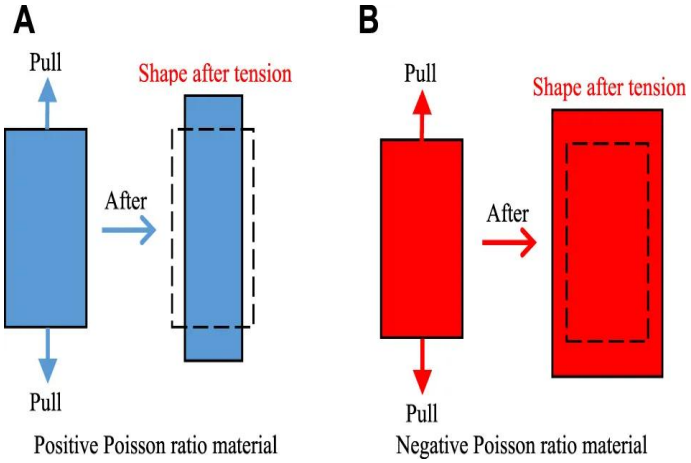


***Figure 6**. Axial tension material deformation. (A) Material with a positive Poisson ratio. (B) Material with a negative Poisson ratio, from [20].*

Auxetic materials exhibit advanced mechanical properties from an engineering perspective due to their negative Poisson's ratio characteristics. When subjected to a point load or an impact, they demonstrate high indentation resistance. During an impact, the auxetic structure contracts toward the center of the impact, increasing its local density in that region and, consequently, its mechanical resistance [21]. Furthermore, these metamaterials exhibit high fracture toughness; as the tensile stresses around a crack formed within the material cause the material to expand in that region, reducing the stress concentration at the crack tip and suppressing micro-crack propagation [21]. Additionally, when auxetic plates are subjected to bending moments, instead of taking an anticlastic shape, they curve bidirectionally and adopt a synclastic form; in other words, the auxetic material forms a dome-shaped structure and provides geometric compatibility without the need for excessive processing or forcing the material to take the desired shape [22].

Auxetic materials are still a developing field. Polyurethane foam with a negative Poisson's ratio, developed by Roderic Lakes in 1987, is considered the first consciously produced auxetic structure [23]. However, it is important not to overlook examples of auxetic materials found in nature. Single crystals of arsenic, cadmium, and iron pyrites are among the most common examples [21]. Also, salamander skin and load-bearing cancellous bone from human shins can be given as examples of biologically found auxetic materials [24] [25]. Figure 7 shows Re-entrant polymer foam with negative Poisson's ratio.

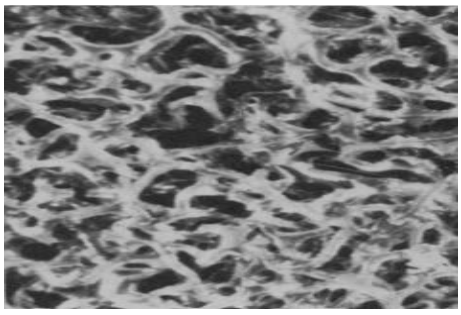


***Figure 7.** Re-entrant polymer foam with negative Poisson's ratio, from [23].*

In general, achieving an auxetic structure is achieved thanks to two factors: a careful selection of the geometries and the deformation mechanism inside the material [26].

1.3. Geometric Classification of Auxetic Materials

Given the importance of the geometry of the cell structures of auxetic materials, it would be appropriate to classify them. There is no single type of classification in the literature. We can group their geometries as re-entrant structures, chiral structures, rotating rigid units, and origami structures [27].

1.3.1. Re-entrant Structures

The term "re-entrant" is used to describe objects that are structurally "oriented inwards" or have a "negative angle". Unlike the outward-facing angles in a standard hexagonal honeycomb structure, in re-entrant geometry the outer ribs point towards the cell center [28]. This inward-facing, negative-angle configuration of the cell walls is a fundamental prerequisite for the material's unusual kinematic response [29]. Realignment of cell ribs at hinges dominates the deformation characteristics of re-entrant structures [30]. Figure 8 shows the re-entrant honeycomb structure.

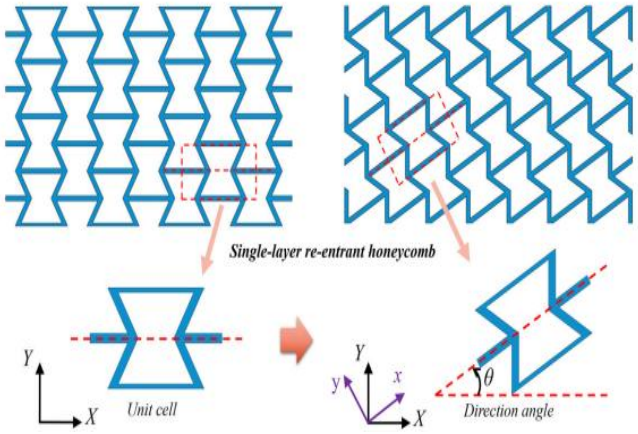


Figure 8. *Re-entrant honeycomb structure and the unit cell, from [31]*

For example, when tensile force is applied to these structures, the inwardly curved arms open outwards from these hinge points, causing an expansion in the overall volume of the material. Figure 9 shows the difference in axial tension deformation between honeycomb and re-entrant honeycomb structures.

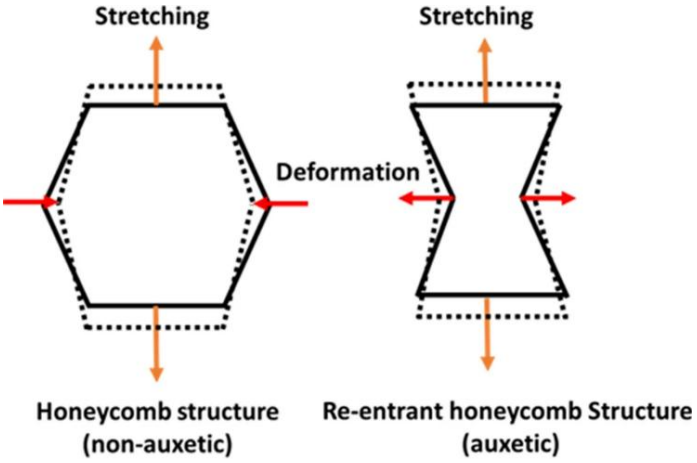


***Figure 9**. Axial tension deformation difference, from [32].*

1.3.2. Chiral Structures

In auxetic materials, chiral structures achieve a negative Poisson's ratio thanks to their asymmetric chirality properties. They consist of two different components: nodes and ligaments. Nodes act as rigid main bodies and are usually circular or ring-shaped. Ligaments are members that connect the nodes to each other. The most important feature of these structures is that the ligaments are tangentially attached to the nodes. This is what gives them chiral properties [33]. Figure 10 shows the tetra-chiral structure.

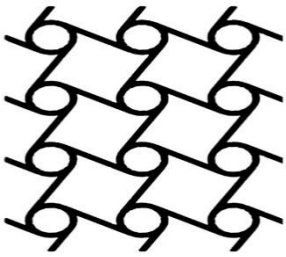


***Figure 10**. Tetra-chiral structure, from [34].*

They achieve auxetic behaviour through node rotation and ligament unrolling mechanisms [35]. When a tensile force is applied to the auxetic chiral structure, the ligaments attempt to open. Because they are tangentially attached to the nodes, the nodes are forced to rotate around their own axes. This causes the structure to expand in all directions, creating the auxetic effect.

1.3.3. Rotating Rigid Units

Rotating rigid units, formed by connecting rigid square, triangular, or rectangular units at their corners with hinges, exhibit isotropic auxetic behaviour when tensile force is applied. The rigid elements begin to rotate around the hinge, expand laterally, and demonstrate auxetic behaviour. Figure 11 shows Rotating rigid squares structure expanding in both axes under tensile stress.

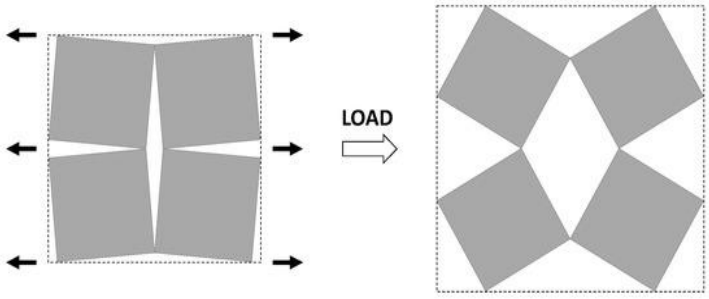


***Figure 11**. Rotating rigid squares structure expanding in both axes under tensile stress, from [36].*

The mechanical properties and auxetic response of these structures depend primarily on the geometry of the units and the angular relationships between them. Their simple designs, repeatable structures, and the ability to exhibit a constant Poisson's ratio close to -1 in multiple loading directions make these systems highly attractive for mechanical applications. Furthermore, it is possible to obtain different auxetic behaviour profiles by changing the geometry of the units and the connection methods [33].

1.3.4. Origami Structures

Origami, a traditional Japanese paper-folding technique, is used in the engineering of auxetic structures due to its ability to increase the system's degree of freedom and provide tunable mechanical responses [27]. These structures are divided into two categories: rigid and deformable structures. In general, these structures exhibit high deformation resistance and mechanical anisotropy, making them ideal for deployable structures [33].

1.4. Considerations on the Choice of Geometry

As previously mentioned, the mechanical properties of auxetic materials stem primarily from their unique geometric arrangements. Re-entrant structures exhibit high energy dissipation capacity and superior out-of-plane strength thanks to the fact that their cell geometries allow for rib bending and rotation [37]. However, a significant disadvantage is that the mechanical responses of these structures vary depending on the direction in which the load is applied due to their anisotropic nature. This limits their use in applications where uniform mechanical performance is critical [38].

When chiral structures are observed, it can be stated that they have both unique advantages and structural limitations. Their Poisson's ratio approaching -1 and superior elongation capacity make them highly suitable for advanced applications requiring high deformation tolerance [39]. The auxetic mechanism observed in chiral systems is based on the rotational movement of circular or cylindrical nodal points integrated with ligaments. However, this high deformation capability brings with it a significant geometric complexity that makes both the design and manufacturing phases quite difficult. Moreover, the structural rigidity of chiral geometries is relatively low [40]. This situation can cause chiral systems to be at a disadvantage in terms of mechanical reliability.

Compared to the above, rotating rigid unit designs such as rotating squares or triangles stand out with their structural simplicity and ideal Poisson's ratio values, as well as their isotropic auxetic behaviour. They are highly suitable for applications requiring equal expansion in all directions under load. Their disadvantage is that, due to the inclusion and reliance on hinges in

their structure, their stiffness and load-bearing capacity are lower than those of other types [41]. They would be more suitable for applications requiring lower load.

Finally, regarding origami structures, they stand out in the literature for their superior adaptability and multi-functionality. Auxetic origami structures not only offer auxetic properties but also significant mechanical advantages such as multi-stability, deployable/foldable forms, and purpose-specific adjustable rigidity profiles. However, the difficulties in the manufacturing process are a major disadvantage in the literature. The performance of origami systems is directly dependent on the characteristic properties of the material and the precision of the folding angles; this makes scaling these designs to practical applications at micro or macro scales quite difficult. Consequently, although these structures can offer a wide range of adjustable Poisson's ratios, their overall mechanical strength is generally weaker compared to traditional auxetic designs [33] [42] [43].

According to these findings in the literature, determining the most suitable auxetic design requires correctly matching the unique advantages offered by each geometry with the specific application requirements. It clearly demonstrates that carefully optimizing structural stiffness, flexibility, manufacturability, and functional diversity parameters to select the most appropriate auxetic architecture is a critical engineering approach for achieving the targeted mechanical performance.

1.5. Bistable Mechanism in Auxetic Materials

Structures operating in an elastic regime deform when a force is applied, but return to their original state like a spring when the force is removed. Consequently, it can be stated that a material with this structure has only one stable state. These structures cause various risks and problems in space applications. For example, a structure to be used in space such as a solar panel, needs to be stable when deployed. However, it is expected to be packed before launch to fit into the rocket. Because the packed state of the structure is unstable, continuous pressure must be applied and locking mechanisms must be used to hold it in that state. The risk of failure of these mechanisms threatens space missions. To overcome this risk, there is a need for next-generation materials that are multistable and exhibit auxetic properties, without the need for a locking mechanism in both the packed and deployed states. Figure 12 shows Bistable and monostable energy landscapes along an elastic energy-displacement curve.

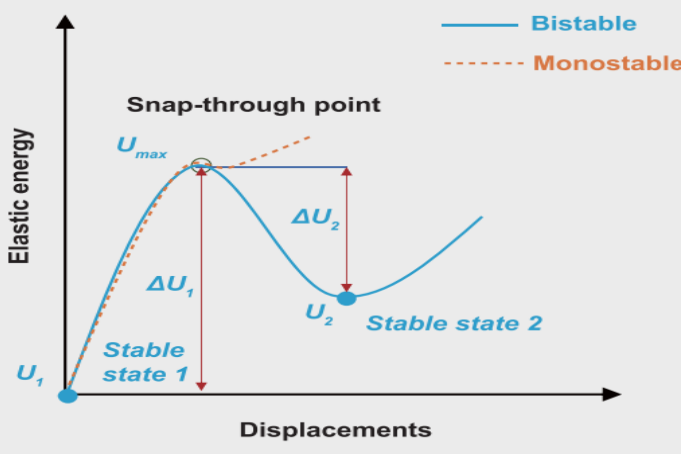


***Figure 12**. Bistable and monostable energy landscapes, from [44].*

When the concept of stability through potential energy-strain curves examined, monostable materials have a single global minimum in their energy curve. The material tends to return to this minimum energy state which is its original shape. In multistable materials, however, there are multiple local minima in the energy curve. Each of these energy wells represents a stable configuration where the structure can maintain its shape without external force. The peaks separating these minimum points represent energy barriers. These are unstable transition states where the system cannot remain in equilibrium. The simplest version of this phenomenon, bistability, occurs when the structure has two distinct stable states [45].

Another important point here is that an external input on the system is required to overcome that energy barrier in the transition between two stable states [46]. This input can be mechanical, thermal or electromagnetic [47]. Even if the applied force disappears after the energy barrier is crossed, the structure does not return to its original state; it settles into its new energy well and remains there. Similarly, provided the material has not suffered plastic deformation, the structure can return from its second stable state to its first stable state if a sufficient external force is applied again.

Multistability and negative Poisson's ratio (NPR) are independent properties. Integrating these properties offers these two unconventional material properties together for aerospace applications and to conduct research on bistable auxetic materials [47]. Designing auxetic materials as bistable structures is still a relatively new area of research. Nevertheless, significant studies exist in the literature. For example, cellular designs inspired by ancient geometric motifs developed by Rafsanjani and Pasini [48] which is shown in figure 13 and mechanisms based on specific rotation angles of rigid units proposed by Shang et al. [49] have been developed to achieve bistable auxetic structures.

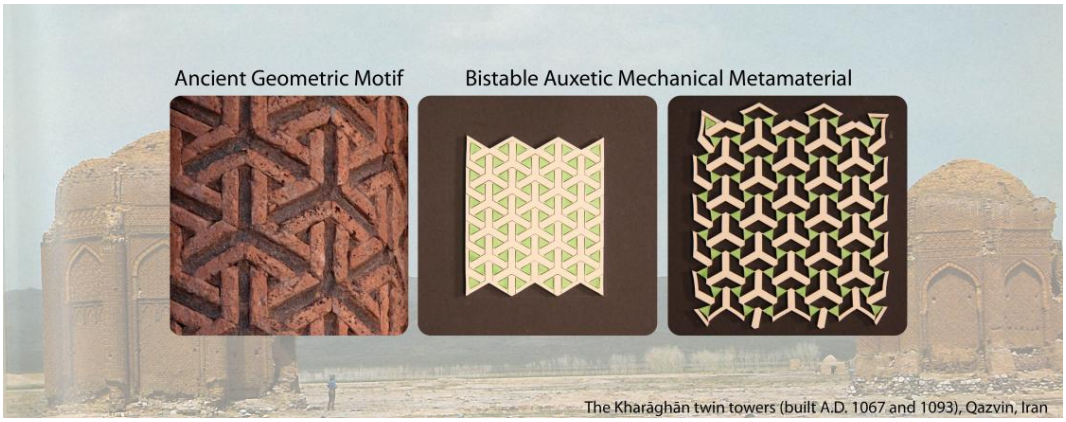


***Figure 13**. Bistable auxetic structures inspired by ancient motifs, from [48].*

Furthermore, foldable origami-based surface designs, offering great potential for deployable structures in space, have also been successfully used to achieve bistable auxetic behaviour by Silverberg et al. [50].

Currently, the production of these designs using advanced manufacturing technologies and their experimental characterization under the mechanical constraints required by space applications constitutes a significant area of research.

1.6. Fabrication Techniques of Auxetic Materials

Various manufacturing approaches are used to fabricate auxetic geometry. Choosing the optimal manufacturing method requires considering the properties of the base material, the desired geometry, and the mechanical properties sought in the final part.

1.6.1. Additive Manufacturing

Additive manufacturing is one of the most common methods used in the production of auxetic materials today. Generally, additive manufacturing involves producing the desired part layer by layer using computer-aided design (CAD) data. Its biggest advantage compared to traditional manufacturing methods is that it offers geometric freedom in production, making it easy to produce complex structures. According to ASTM standards, additive manufacturing techniques are classified as Material Extrusion (FDM/FFF), Powder Bed Fusion, Sheet Lamination, Directed Energy Deposition (DED), Vat Photopolymerisation (VAT), Material Jetting, and Binder Jetting [51]. The selection of the most appropriate AM (Additive Manufacturing) method primarily depends on the target application and the base material. Today, AM processes can be used with a wide range of materials, from polymers (e.g., TPU, PLA) to metal alloys (e.g., Ti6Al4V) and ceramics. This versatility allows them to meet the demands of next-generation applications across various sectors.

The complex and re-entrant geometries found in auxetic materials are quite difficult to produce using conventional manufacturing methods. AM technologies have enabled the highly precise production of these structures. Furthermore, AM allows for the manipulation of the material's internal structure. Thanks to CAD software and algorithmic designs, cellular parameters (ligament thickness, cell angle, etc.) can be locally tailored. This allows for the production of materials with a tunable Poisson's ratio. On the other hand, in many applications, they are at a disadvantage compared to conventional manufacturing methods in terms of processing time and cost.

Among various additive manufacturing techniques, the specific method used in this study is Fused Deposition Modeling (FDM), also known as Fused Filament Production (FFF). The Fused Deposition Modeling (FDM) process creates 3D objects by melting and reshaping raw materials. A drive wheel pulls spooled filament into a heated nozzle, which warms the plastic to a semi-liquid state. Guided by digital instructions from CAD software, the nozzle deposits this extruded material in stacked layers to build the final part [52]. Figure 14 shows a schematic of the FDM/FFF process.

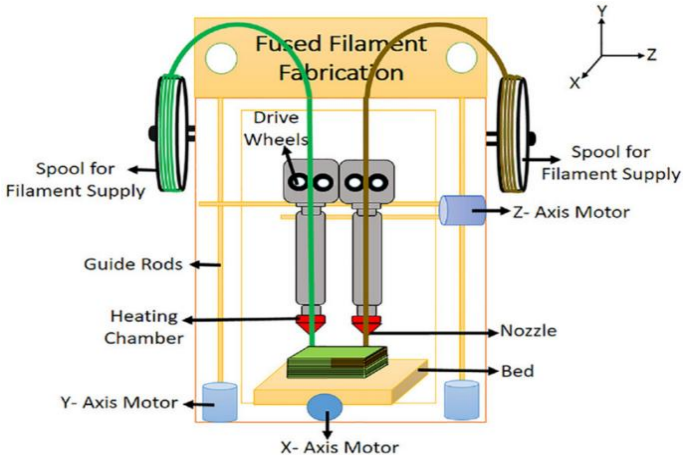


Figure 14. *Schematic of the FDM/FFF process, from [53]*

Filaments serve as the fundamental feedstock for Fused Deposition Modeling. While these are typically composed of polymers with relatively low melting temperatures, specific engineering applications often require reinforcing the base material to enhance its overall mechanical strength [54]. This manufacturing approach provides significant benefits, including minimized material waste, lowered production expenses, and the capacity to fabricate intricate geometries. Furthermore, its highly automated, low-labor nature has facilitated its rapid expansion and adoption across diverse engineering disciplines [55].

Since FDM/FFF builds objects layer by layer, the filament's thermoplastic characteristics are essential for proper bonding and cooling. Processing variables such as layer thickness, extrusion width, and print orientation heavily influence the mechanical strength of the final product and cause anisotropy. Balancing these strict requirements makes developing new FDM filaments quite difficult [56]. When designing auxetic materials, this anisotropic behaviour must be carefully considered, and it must be ensured that the primary loading axes are aligned with the stronger load-bearing planes.

FDM/FFF enables the fabrication of these complex and multi-rigidity topological designs required for next-generation deployable space structures.

1.6.2. Laser Cutting

Laser cutting is a highly precise and versatile manufacturing method that shapes materials by using a focused beam of light to melt, burn, or vaporize them [57]. The main reason why it is frequently preferred in many fields such as manufacturing, design and prototyping is its ability to provide smooth and clean cuts even in the most complex patterns. Lasers are classified according to their interaction with the material. The three most basic methods are fusion cutting, flame cutting and sublimation cutting. This production method, which works on a very wide range of materials from metals such as steel and aluminum to acrylic, wood, glass, fabric and paper, eliminates the risk of material damage with its contactless nature, while offering high-speed production with minimum waste.

Its high precision in cutting planar surfaces makes it highly suitable for the production of sheet-based auxetic materials. However, it may not offer the same ease and flexibility in the production of complex three-dimensional structures [33].

1.6.3. Auxetic Foam Fabrication

Auxetic foams are obtained by structurally modifying conventional foam matrices through methods such as thermo-mechanical compression, volumetric compression, or chemical expansion [58]. In thermo-mechanical compression, commonly applied to polymeric materials such as polyurethane and polyethylene, the foam material is compressed at elevated temperatures and then cooled to fix the re-entrant structure at the cellular level. In volumetric compression, multiaxial mechanical force is applied to the material to obtain a negative Poisson's ratio. Alternatively, in chemical expansion, porous networks with auxetic characteristics are formed through chemical reactions.

While bulk auxetic materials generally offer significant advantages for scalable and cost-effective production, they also lead to limited control over microstructural complexity [33].

2. Design of Auxetic Structures

This section presents the design of a bistable auxetic material, inspired by the work carried out in reference [48]. It was considered appropriate to design rotating rigid square units for this study. The main objective is to create a cell model that allows for parametric evaluation of the effect of geometric properties on the mechanical response of the material. Altair Inspire software was used in the computer-aided design (CAD) process.

The analysis is based on first modeling a single isolated unit cell and then extending this model to multi-cell systems. A square block has been chosen as the reference geometry. Figure 15 shows a 2D square cell design.

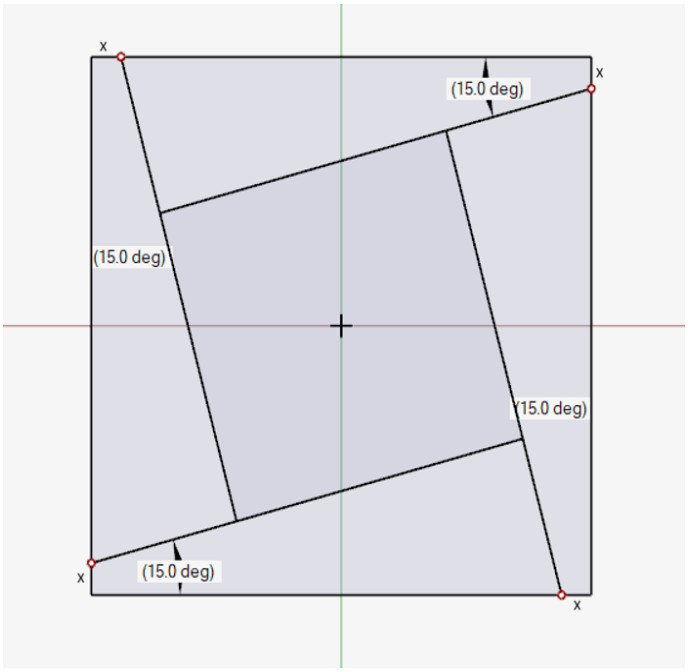


Figure 15. *Designed square block model*

The corner angles, shown as 15 degrees in Figure 15, are defined as cell angles. The cell angle, which is used to obtain the central rotating unit, is the inclination angle of the lines that indicate the material's cutting segments in a basic block. For the reference model, the cell angle was taken as 15 degrees. The value of the cell angle is quite important and has maximum limits. Since the cell in our study is square, the cell angle cannot exceed 45 degrees. This is because at angles greater than 45 degrees, the square cell formed in the center, which provides the rotational movement, disappears. Therefore, the angle should be kept below 45 degrees. The X values shown in Figure 15 represent the variation of the deviation of the cutting lines from the vertices. This length cannot be considered independently of the cell angle and is an important parameter for the structure. It was determined as 3 mm in the reference design. Subsequently, this design was extruded to create a 3D model.

Figure 16 shows a 2D drawing of the flexible hinge design that enables the rotational movement of the squares. The value shown as 0.8 mm represents the hinge thickness, and the value shown as 3.75 mm represents the hinge length. These values were taken from the

reference model. Variations in hinge design, especially differences in thickness, constitute an important parametric study for the bistable mechanism.

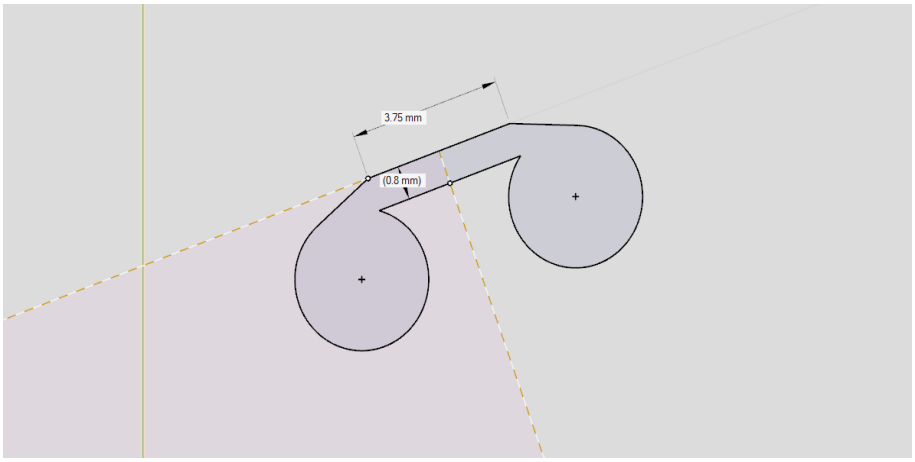


Figure 16. *Flexible hinge design*

The cell topology designed after the 3D-generated square and hinge designs is shown in Figure 17.

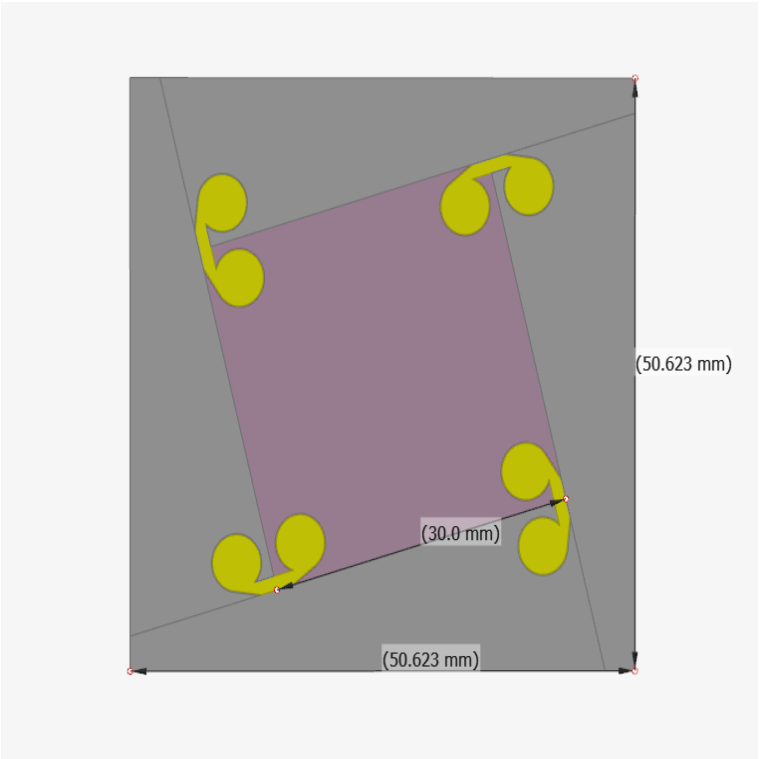


Figure 17. *Design of the single square unit cell*

In the presented cell topology, the central purple region represents the rigid square unit undergoing rotational movement, while the surrounding gray areas represent the main rigid outer structure. The yellow curved structures form the flexible hinges that enable the rotational kinematics of the central square unit relative to the outer structure.

After completing the topological design of the isolated unit cell, multiple cell matrices were created to investigate the mechanistic behaviour at the macroscopic level. The main objective here was to measure how increasing the cell count changes the auxetic character, bistable behaviour, and stiffness of the structure. Accordingly, the basic cell was replicated using mirroring operations in the Altair Inspire software. The 2x2 (4 unit cell) and 4x4 (16 unit cell) systems designed within the scope of this study are shown in Figure 18 and Figure 19, respectively.

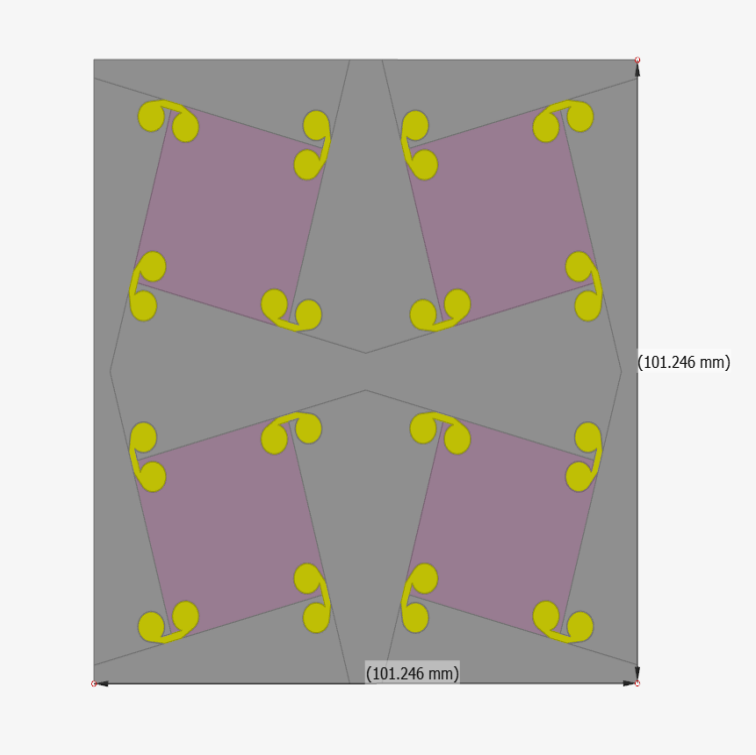


Figure 18. *2x2 matrix cell consisting of 4 square cells*

The number of cells was increased to examine whether the structure exhibits homogeneous auxetic behaviour at the macroscopic level.

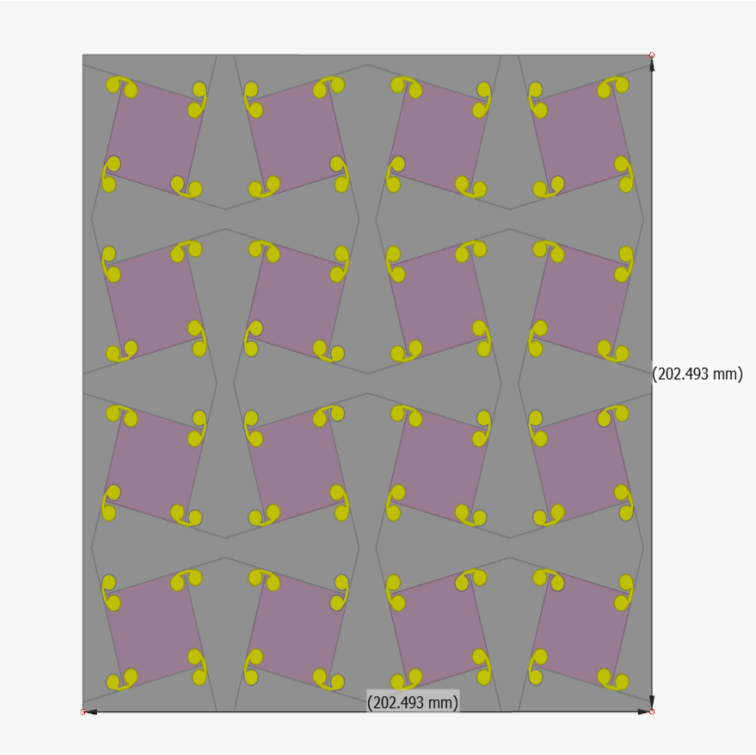


Figure 19. *4x4 matrix cell consisting of 16 square cells*

In addition to the cell design, rigid end tabs have been integrated into the design to compensate for the lateral pressure applied by the grips of the testing device during tensile testing of the multicellular structure. This modification, shown in Figure 20, ensures that the applied axial load is transferred homogeneously to the test area of the specimen and minimizes the risk of premature failure due to stress concentrations that may occur in the grip areas.

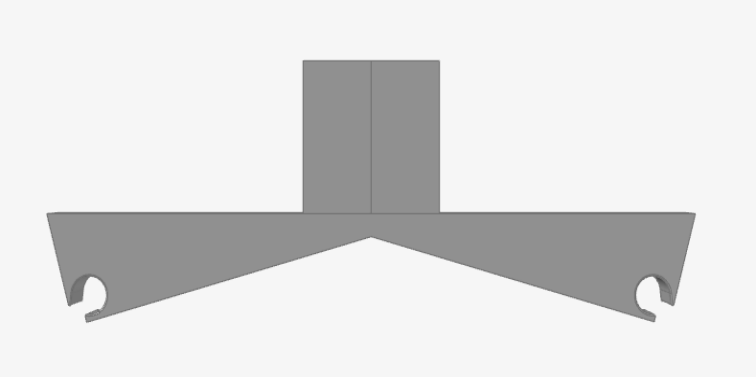


Figure 20. *Rigid end tab design for axial tensile test*

Following the completion of the geometric modeling phase, the prototyping process for physical testing of these structures has begun.

3. Materials, Manufacturing and Prototyping

3.1. Selection of Manufacturing Method

In this study, FDM/FFF (Fused Deposition Modeling / Fused Filament Fabrication), an additive manufacturing method, was chosen for the prototyping of the designed rotating rigid squares auxetic material. This choice is based on both geometric and mechanical reasons. As mentioned above, auxetic materials have complex internal designs and cellular structures to achieve a negative Poisson's ratio. Producing such complex geometries with traditional manufacturing methods is not feasible due to both geometric limitations and high costs. Therefore, additive manufacturing was considered appropriate in this study. Thanks to its layer-by-layer manufacturing logic, the FDM method allows for rapid prototyping of these complex geometries at low cost.

3.2. Multi-Material Requirement

In rotating rigid unit designs, hinges and rotating units exhibit different mechanical responses to applied forces due to their differing functions. The components forming the system's skeleton and the rotating squares must maintain their shape and perform rotational movement under tensile stress. Therefore, PLA, a thermoplastic with a high modulus of elasticity and yield strength, was chosen. The hinges connecting the rigid squares and forming the axes of rotation must accommodate elongation and angular changes to facilitate the structure's overall negative Poisson's ratio. For these reasons, TPU, which has high elongation at break and flexibility values, was used to obtain connection points with a high fatigue life and behaving like a true hinge. In contrast, in auxetic geometries made from a single material, undesirable deformations can be observed in areas requiring rigidity, and sudden fractures can occur in areas requiring flexibility.

3.3. Process Parameters and Challenges

For the Additive Manufacturing process, the Bambu Lab A1 mini 3D printer was chosen, and for the slicing operations, the Bambu Studio software was selected. The 3D printer used in this study is shown in Figure 21. The FDM process parameters are given in Table 1.

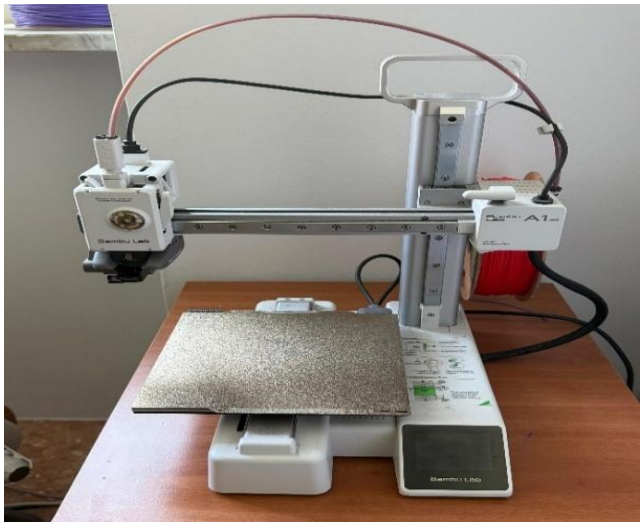


Figure 21. *Bambu Lab A1 Mini 3D Printer*

***Table 1**. FDM process parameters*

Material Grade	Nozzle diameter (mm)	Layer height (mm)	Infill density (%)	Printing temperature (°C)	Printing Speed (mm/s)	Raster orientation (°)	Build orientation
Tough PLA	0.4	0.2	15	220	200	45	Flat
TPU 95A	0.4	0.2	15	230	31	45	Flat

Considering that the device did not have a dual-extrusion system, an alternative manufacturing strategy was developed. According to this strategy, rigid PLA squares and other rigid components, alongside flexible TPU hinges, were fabricated on separate build plates instead of simultaneously. To achieve the targeted multi-cell architecture, the fabricated flexible hinges were integrated into the designated cavities of the rigid framework, facilitating the mechanical interlocking of the components. This sequential fabrication and assembly approach successfully yielded the designed multi-cell structure.

For the mechanical parametric study to be conducted, specimens with different structures were produced. Specimens produced with different hinge thickness and cell angle values are listed in tables 2 and 3, respectively.

***Table 2.** Parametric combinations of specimen cell sizes and hinge thicknesses*

Specimen Cell Size	Hinge Thickness (mm)
2x2	0.8
2x2	1.2
2x2	1.6
4x4	0.8
4x4	1.2
4x4	1.6

***Table 3**. Parametric combinations of specimen cell sizes and cell angles.*

Specimen Cell Size	Cell Angle (Degree)
2x2	10
2x2	15
2x2	20
2x2	25

One of the primary challenges encountered during the assembly phase was the dimensional deviation characteristic of FDM 3D printing, specifically the inward shrinkage of the cavities within the rigid PLA matrix. Both materials experience thermal shrinkage during cooling but the reduction in the internal dimensions of the PLA cavities prevents the standard-sized TPU hinges from fitting correctly. To resolve this without changing the PLA design, a negative dimensional offset of 0.1 mm was applied to the outer contours of the TPU hinges. This adjustment combined with the elastomeric nature of TPU, allowed the flexible hinges to

elastically deform during insertion, thereby creating a reliable press-fit. Optimal mechanical interlocking was achieved, ensuring the structural integrity of the multi-cell specimens before mechanical testing. A hinge design with a negative dimensional offset operation is shown in Figure 22.

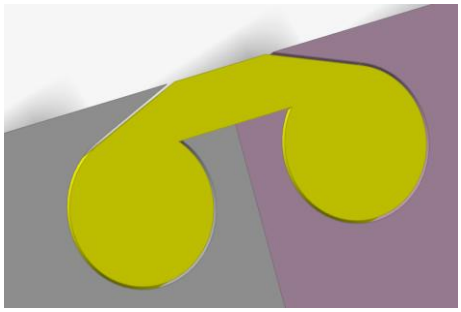


Figure 22. *Negative dimensional offset operation applied to hinge design*

To visually demonstrate the kinematic mechanism of the design prior to mechanical testing, Figure 23 and 24 illustrates the physical prototype in both its initial configuration and its fully deployed state. The deployed geometry clearly exhibits the auxetic behaviour driven by the rotation of the rigid PLA units and the elastic deformation of the TPU hinges.



Figure 23. *The physical prototype of the multi-cell structure*

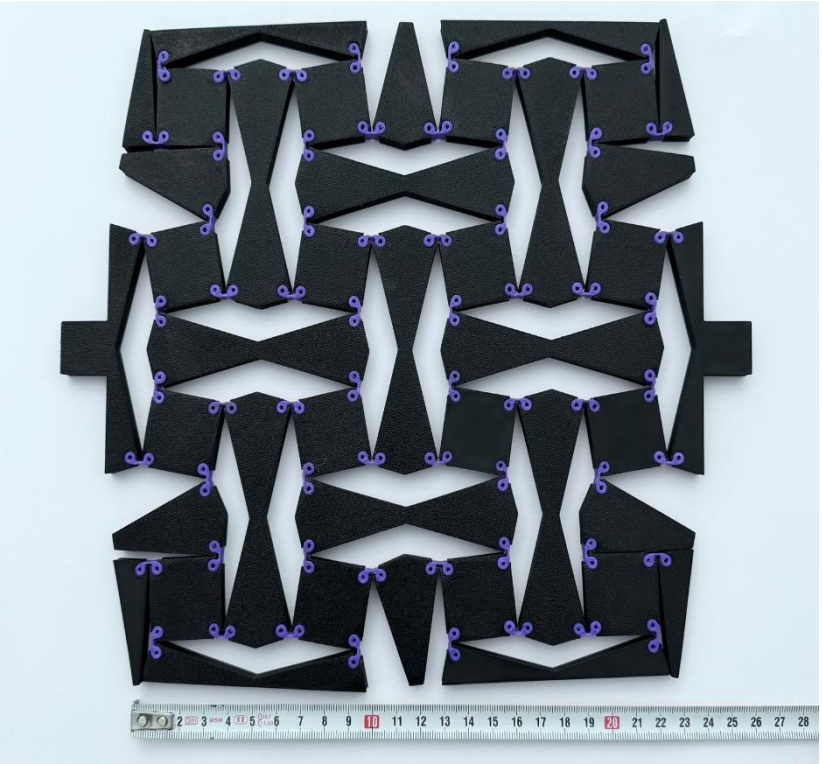


Figure 24. *The physical prototype of the multi-cell structure in the fully deployed state.*

The prototype is shown in its final state, including the integrated end tabs, ready for the uniaxial tensile testing setup.

4. Mechanical Characterization and Testing

4.1. Mechanical Testing Setup

Uniaxial tensile tests were performed to characterize the mechanical behaviour and auxetic properties of the produced multi-cell prototypes. The experiments were conducted in a 5 kN capacity Instron Single Column Universal Testing Machine in displacement-controlled mode. Figure 25 shows the 4x4 matrix sample placed in the tensile testing machine.

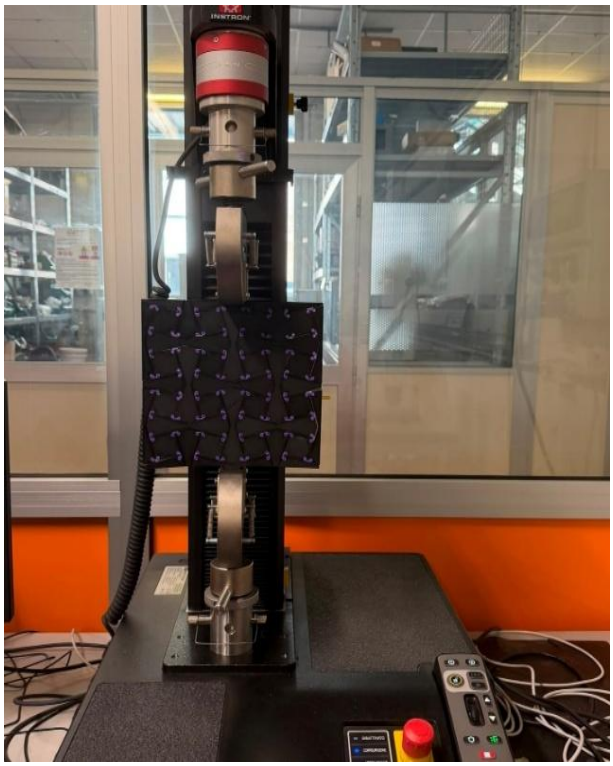


Figure 25. *Uniaxial tensile testing experimental setup for 4x4 matrix design.*

Test parameters were scaled according to sample dimensions; samples with a 2x2 matrix structure were tested with a maximum displacement of 35 mm, and samples with a 4x4 matrix structure were tested with a maximum displacement of 70 mm. While six different 2x2 matrix configurations were tested, only three different cell configurations with 4x4 matrices were tested. End tabs were used to prevent damage to the grip areas of the sample during the test, and all tests were completed at room temperature at a constant tensile speed of 30 mm/min. The applied force and displacement data were recorded simultaneously with the device's own data acquisition system. Figure 26 shows the state of the 4x4 matrix specimen placed in the tensile testing machine at the end of the test.



Figure 26. *Deployed structure of the multi-cell prototype after tensile testing.*

Testing only one specimen per configuration is still a constraint, even though the initial findings from the nine distinct examined configurations offer insightful information. Multiple replicates should be used in future research to determine statistical significance.

4.2. Testing Results

In order to systematically evaluate the influence of structural parameters on the global kinematic and mechanical behaviour of the auxetic prototypes, the uniaxial tensile test results are categorized into three distinct parametric studies. First, the effect of hinge thickness is analyzed on 2x2 matrix specimens to observe fundamental bistable mechanics at a smaller scale. Then, the impact of varying cell angles (10°, 15°, 20°, and 25°) is investigated within the same 2x2 configuration to determine the role of initial geometric rotational limits. In the end, the analysis is scaled up to 4x4 multi-cell matrices to assess how hinge thickness variations impact in a globally deployed macroscopic structure.

4.2.1. 2 x 2 Specimens with Different Hinge Thicknesses

After standardizing the test setup, the initial test was designed to quantitatively evaluate the effect of different hinge thicknesses on the cellular mechanism and overall mechanical behavior in 2 x 2 specimens. In this analysis, all other parameters constituting the basic geometry of the structure were kept constant as control variables. The fixed reference values are as follows:

Side length of the rotating rigid squares: 30.0 mm

- Variation of the deviation of the cutting lines from the vertices: 3.0 mm

- Cell angle: 15°

- Hinge length: 3.75 mm

Three different hinge thicknesses were designed as independent variables: 0.8 mm, 1.2 mm, and 1.6 mm. 3D manufacturing of these three designs was completed using optimized parameters, and the samples were subjected to uniaxial tensile testing under the standard conditions detailed earlier.

Following the completion of the tensile tests, simultaneous force-displacement data obtained from the device were compiled and a comparative analysis was presented. This data quantitatively reveals the effect of hinge thickness, chosen as an independent variable, on the bistable behaviour and global stiffness of the structure. Figure 27 shows the initial configuration of the sample with a 2x2 matrix in the tensile testing machine.



Figure 27. *The initial configuration of the 2x2 multi-cell specimen mounted in the universal testing machine.*

In Figure 28, the tensile test results of three different configurations of a 2x2 multicell matrix structure and hinge thicknesses of 0.8 mm, 1.2 mm and 1.6 mm are presented on a single graph.

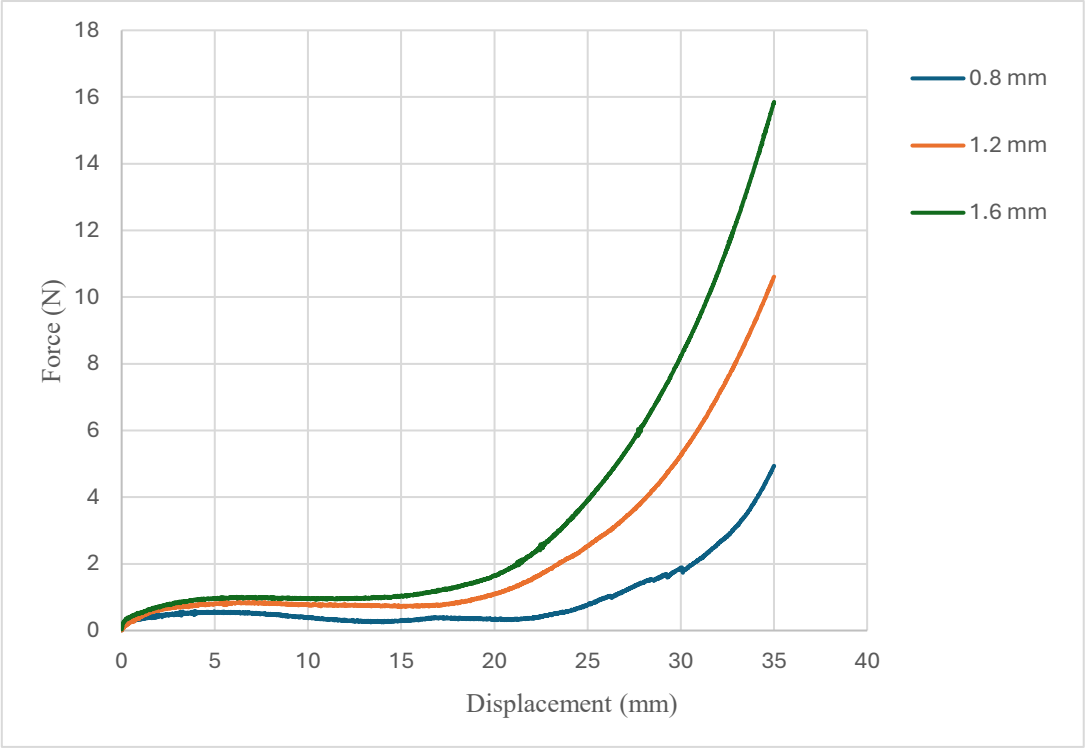


Figure 28. *Force-displacement curves of 2x2 specimens.*

The enlarged force-displacement plot (Figure 29) details the initial kinematic response of 2x2 multi-cell structures with different hinge thicknesses. The 0–14 mm displacement region represents the critical elastic energy barrier and the onset of structural rotation before geometric locking occurs. To calculate the initial stiffness of the structures, a linear fit was applied where the force-displacement response remains linear before the rotation mechanism becomes dominant.

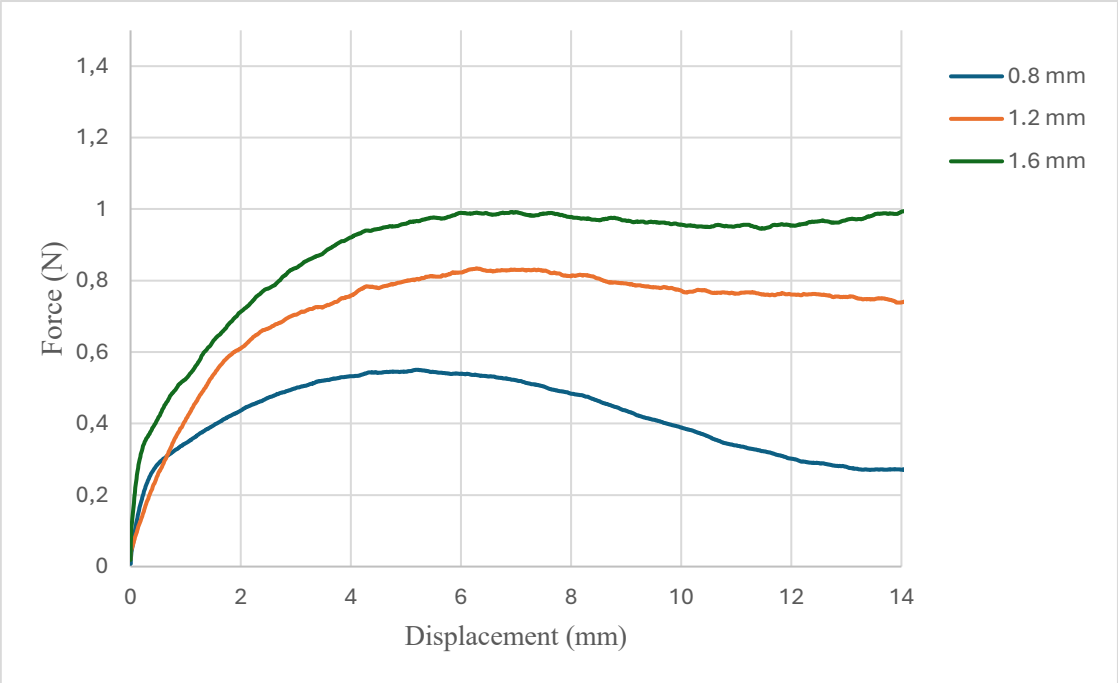


Figure 29. *Enlarged view of the force-displacement curves in the initial displacement region (0-14 mm) for 2x2 specimens with varying hinge thicknesses.*

The initial stiffness of the specimen containing a 0.8 mm thick hinge was estimated 0.11 N/mm. The structure reaches an initial peak force of approximately 0.55 N at a displacement of approximately 5 mm. After this threshold is exceeded, negative stiffness occurs with a snap-through response, and the force decreases to levels of 0.25 N. The negative stiffness behaviour supports the specimen exhibiting bistable-like behaviour.

The initial stiffness of the sample with a 1.2-mm-thick hinge was estimated 0.20 N/mm. Compared to the previous 0.8 mm sample, it reaches its peak force at a larger displacement. At a displacement of around 6 mm, it attains an initial peak force of approximately 0.85 N. The subsequent force drop is less pronounced, indicating that the thicker hinge generates higher restoring forces.

The initial stiffness of the specimen containing a 1.6 mm thick hinge estimated 0.24 N/mm. Between 6-8 mm of displacement, the force peaks at 1 N and subsequently exhibits almost neutral stiffness behaviour. This lack of a significant negative stiffness drop suggests that the high strain energy stored in the thick hinge suppresses the snap-through mechanism, and the structure exhibits a monostable tendency rather than a bistable response.

The instantaneous derivative at each point was calculated by determining the slope of the force-displacement curve. Since these derivative values represent stiffness, instantaneous stiffness curves were generated (dF/dx). To quantitatively evaluate the kinematic response of 2×2 multi-cell matrices, instantaneous stiffness (dF/dx) profiles were analyzed. Figure 30 presents these derivative profiles for samples with different hinge thicknesses, mathematically shows the mechanics behind the elastic energy barrier.

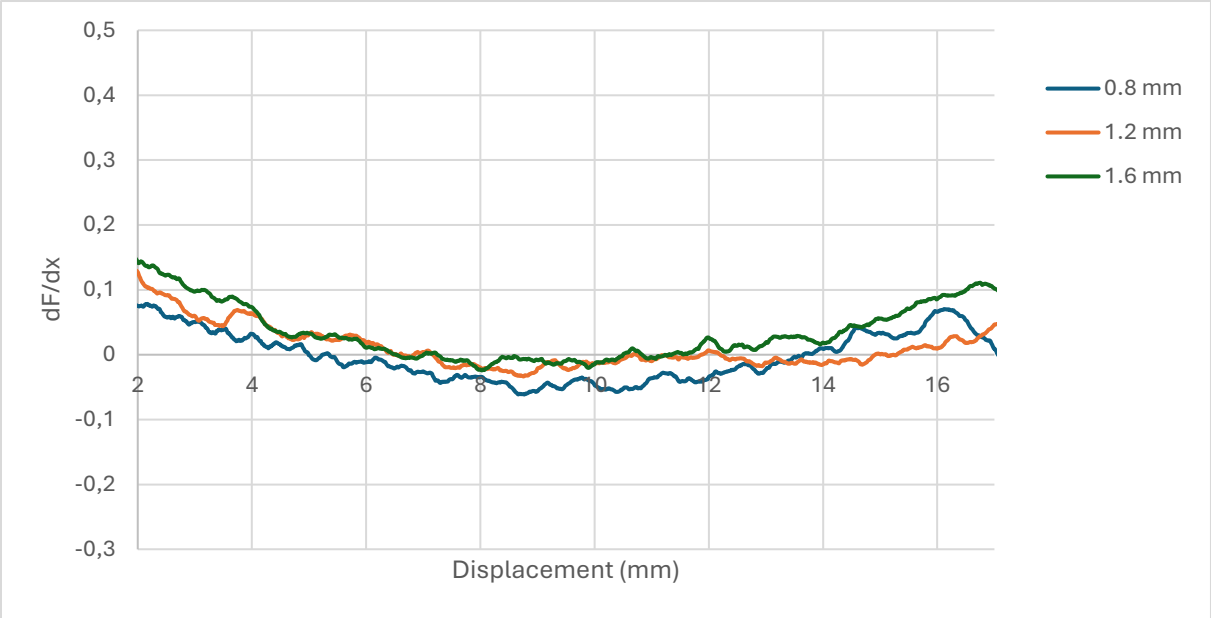


Figure 30. *Instantaneous stiffness (dF/dx) profiles as a function of displacement for 2×2 multi-cell matrices with varying hinge thicknesses (0.8 mm, 1.2 mm, and 1.6 mm).*

For the specimen with a 0.8 mm hinge, the instantaneous stiffness curve exhibits a distinct transition to the negative stiffness regime. At approximately 5 mm displacement, the derivative curve intersects the horizontal zero axis downwards, reaching the peak force point and mathematically confirming the initiation of the snap-through mechanism. The curve reaches a clear and continuous local minimum between 7 mm and 12 mm, proving that the thin hinges allow the structure to successfully overcome the elastic energy barrier and transition to the deployed state.

The derivative curve of the specimen containing a 1.2 mm thick hinge intersects the x-axis at ~6 mm, creating a significantly shallower negative trough. This weakened negative stiffness indicates that the increased hinge thickness generates higher restoring forces, thus weakening the snap-through capability of the cellular matrix.

In contrast, the derivative profile of the 1.6 mm specimen, containing the thickest hinges, only briefly and shallowly intersects the zero line. Although a marginal negative stiffness region is observed, the high strain energy stored in the hinges severely suppresses the snap-through mechanism. Consequently, the structure is prevented from securely locking into a secondary stable energy well, forcing the macroscopic 2x2 matrix to exhibit a predominantly monostable kinematic tendency.

During the rotation phase (0-20 mm), while the axial tensile force compelled the rigid squares to rotate, the structure exhibited lateral expansion at the macroscopic level, demonstrating its characteristic negative Poisson's ratio behaviour. Figure 31 shows the rotational phase of a 2x2 matrix.



Figure 31. *The intermediate rotational phase of the 2x2 specimen during uniaxial tension.*

The total opening energy required to fully deploy the mechanism and achieve geometric locking can be calculated by determining the area under the force-displacement curve. Examination of the data reveals a direct correlation between this energy and hinge thickness. The structure of a 0.8-mm hinge requires a lower energy threshold, while the stiffer structure of a 1.6-mm hinge demands significantly higher energy for deployment. This is a critical parameter for motor sizing and energy budget estimations in deployable systems for space applications.

The curve in Figure 32, which provides a detailed view of the 19–37 mm displacement range, reflects the post-deployment phase where the 2x2 matrix structure completes its rotational movement, reaches geometric locking, and subsequently exhibits macroscopic tensile behaviour.

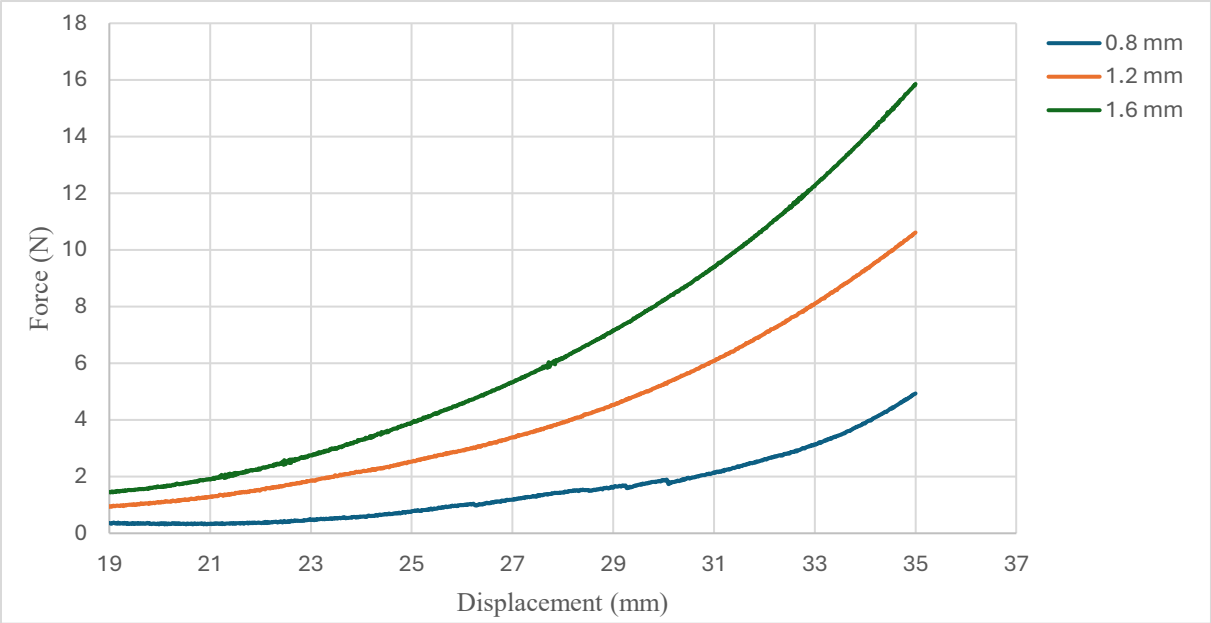


Figure 32. *Enlarged view of the force-displacement curves in the final deployment region (19-35 mm) for 2x2 specimens with varying hinge thicknesses.*

After 20 mm displacement, the rigid PLA squares have reached their geometric rotation limits, resulting in structural locking. Beyond this point, the system starts to behave as a cellular mechanism and transforms into a monolithic structure undergoing axial tension.

At the maximum displacement of 35 mm, where the test ends, the effect of hinge thickness on global force resistance becomes apparent. While the 0.8 mm thick sample reaches at approximately 5 N, the 1.2 mm sample reaches ~10.5 N, and the 1.6 mm thick sample reaches a load-carrying capacity of approximately 16 N. This supports the finding that increasing the thickness directly increases global stiffness.

The sample with thicker hinges exhibited higher stiffness in the final structure is observed. The significantly higher calculated final stiffness value in this region numerically demonstrates the much stronger structural integrity of the deployed structure compared to thinner hinges.

Figure 33 shows the deployed state of the sample with a 2x2 matrix at the end of the tensile test.

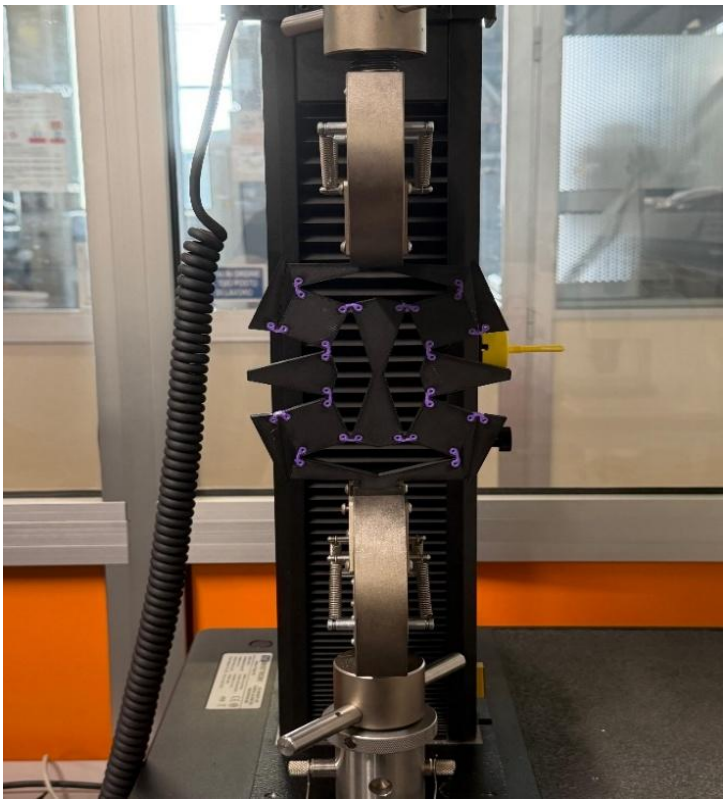


Figure 33. *The fully deployed and geometrically locked configuration of the 2x2 specimen.*

All critical parameters obtained from the kinematic and structural analyses are presented in Table 4 to summarize the effect of hinge thickness.

Table 4. *Summary of key mechanical properties for 2x2 specimens with varying hinge thicknesses.*

Hinge Thickness (mm)	Initial Stiffness (N/mm)	1st Peak Force (N)	Displacement at Peak (mm)	Stiffness at 35 mm (N/mm)	Max Load at 35 mm (N)
0.8	0.11	~0.55	~5	1.00	~5.0
1.2	0.20	~0.85	~6.0	1.22	~10.5
1.6	0.24	~1.00	~6.0 - 8.0	1.70	~16.0

4.2.2. 2 x 2 Specimens with Different Cell Angle

After standardizing the test setup, tensile tests were performed on 2 x 2 specimens to quantitatively evaluate the effect of different cell angles on cellular mechanisms and overall mechanical behaviour. In this analysis, all other parameters constituting the basic geometry of the structure were kept constant as control variables. The fixed reference values are as follows:

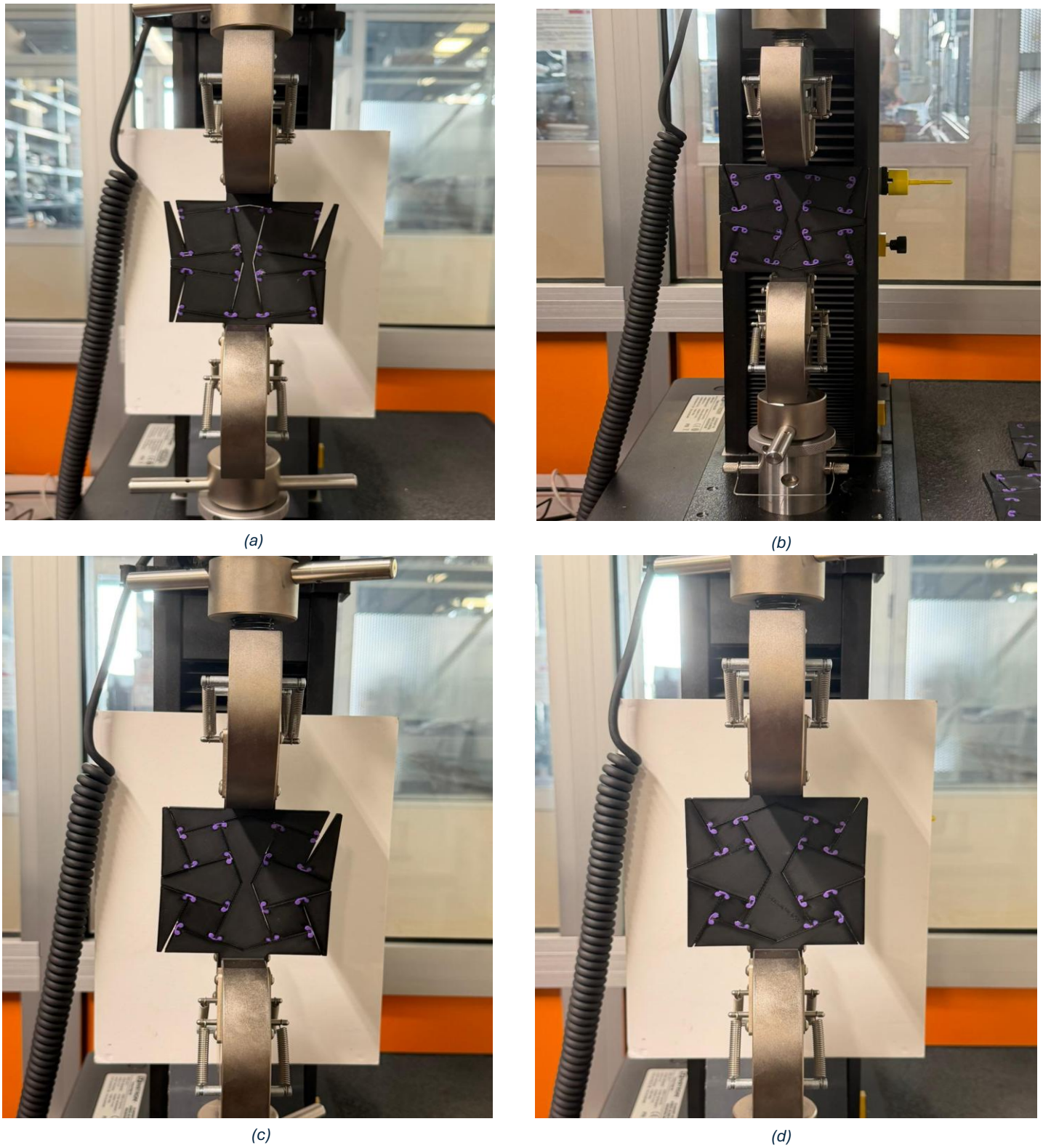
- Variation of the deviation of the cutting lines from the vertices: 3.0 mm

- Hinge thickness: 0.8 mm

- Hinge length: 3.75 mm

Four different cell angles were designed as independent variables: 10°, 15°, 20°, and 25°. 3D manufacturing of these four designs was completed using optimized parameters, and the samples were subjected to uniaxial tensile testing under the standard conditions detailed earlier.

Figure 34 shows a model of samples containing cell angles of 10°, 15°, 20°, and 25°. These images clearly demonstrate that the change in cell angle significantly affects the area of the rotational squares in the model. As the angle increases, the rigid squares inside become smaller.



(a) (b) (c) (d)

Figure 34. *The appearance of samples with different cell angles: (a) 10°, (b) 15°, (c) 20° and (d) 25°.*

Following the completion of the tensile tests, simultaneous force-displacement data obtained from the device were compiled and a comparative analysis was presented. This data quantitatively reveals the effect of cell angle, chosen as an independent variable, on the bistable behaviour and global stiffness of the structure.

In Figure 35, the tensile test results of four different configurations of a 2x2 multicell matrix structure and cell angles of 10°, 15°, 20° and, 25° are presented on a single graph.

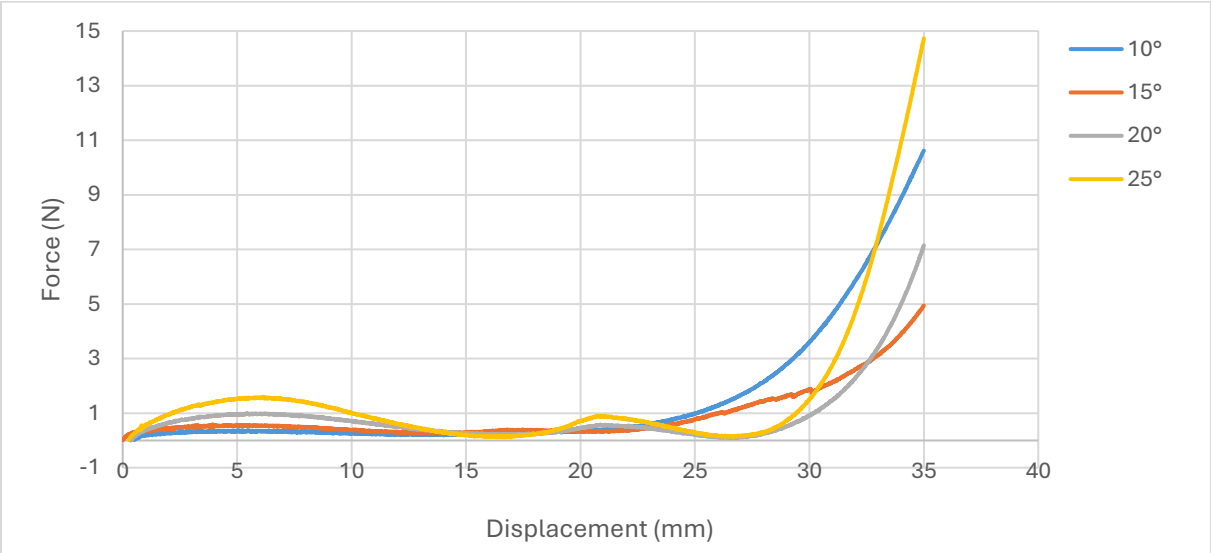


Figure 35. *Tensile test results comparing the force-displacement behaviour of 2x2 multicell matrix structures configured with cell angles of 10°, 15°, 20°, and 25°.*

The enlarged force-displacement plot (Figure 36) details the initial kinematic response of 2x2 multi-cell structures with different cell angles. The pronounced behaviour, particularly at 20° and 25° cell angles, indicates a fundamental shift in the kinematic mechanism, signaling a transition from simultaneous opening to a sequential structural release.

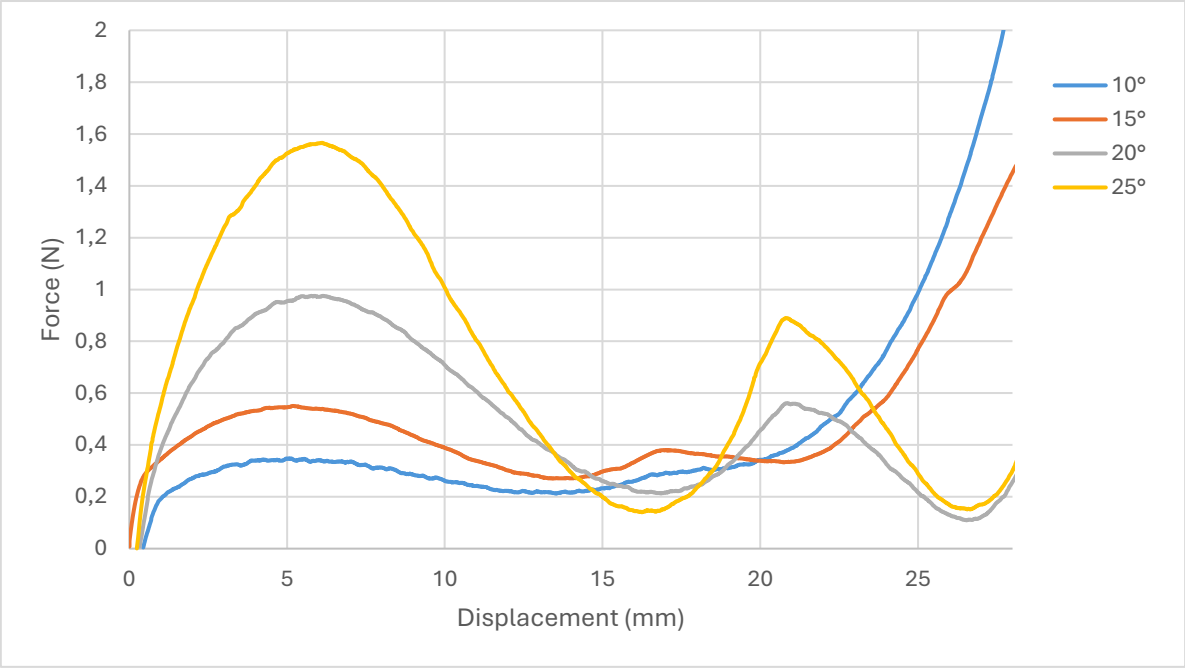


Figure 36. *Enlarged view of the initial force-displacement response for 2x2 multi-cell structures with cell angles of 10°, 15°, 20°, and 25°.*

As the cell angle increases from 10° to 25°, the initial peak force required to trigger the rotation mechanism increases significantly. A sample with a 10° cell angle reaches approximately 0.35 N peak force at a displacement of about 5 mm. It subsequently exhibits negative stiffness with a force decrease but this decrease appears quite shallow. Its snap-through mechanism is not very strong. For the 15° cell angle, the peak force is again approximately 0.55 N with a displacement of about 5 mm. After this peak, it smoothly decreases to a local minimum of around 0.25 N. A sample with a cell angle of 20° reaches a peak force of approximately 0.95 N at approximately 6 mm. A sample with a cell angle of 25° reaches a peak force of approximately 1.55 N at approximately 7 mm.

As a result of the applied linear fit process, the initial stiffness values of the 10°, 15°, 20°, and 25° specimens were estimated to be 0.07, 0.11, 0.48, and 0.49 N/mm, respectively. The 25° specimen requires a much higher elastic energy input to overcome its geometric resistance in order to perform a snap-through mechanism, indicating a much higher initial stiffness.

Increasing the cell angle directly determines the size of the rotating square formed at the center of the base block by increasing the slope of the cut-off lines. This is not just a static shape change, but a critical kinematic parameter that alters the dynamic load-carrying capacity and behaviour of the structure. As the angle increases, the cut-off lines move closer to the center, reducing the size of the inner squares. When the rigid squares at the center are reduced while the outer dimensions of the cell are kept constant, the movement areas and voids within the system expand. In models with smaller angles, such as 10° or 15°, there are almost no voids in the structure because the rotating rigid large squares inside are positioned very close together. When the angle increases to 25°, the increased voids add structural tolerance to the system.

In structures with small angles, when an axial tensile force is applied, it has been observed that the force is transmitted to all cells almost instantly because the large squares provide little space for movement. In particular, in a specimen with a 10° cell angle, four cells begin to rotate almost simultaneously, overcome the energy barrier together, and create the nearly neutral

behaviour shown in the graph below. In structures with large angles, however, the increased internal voids due to the small squares prevent the instantaneous spread of force throughout the matrix. While the cells closest to the tensile grips begin to move and approach their rotational limits, the other cells have not yet reached maximum stress due to this increased void tolerance. Due to the nature of the tensile test, the first drop in the graph is observed when the top row group of cells overcomes its energy barrier and creates a snap-through mechanism; then the load is transferred to the next group of cells, and when they also overcome their barriers, the second valley is formed.

The instantaneous derivative at each point was calculated by determining the slope of the force-displacement curve. Since these derivative values represent stiffness, instantaneous stiffness curves were generated (dF/dx). To quantitatively evaluate the kinematic response, instantaneous stiffness (dF/dx) profiles were analyzed. Figure 37 presents these derivative profiles for samples with different cell angles.

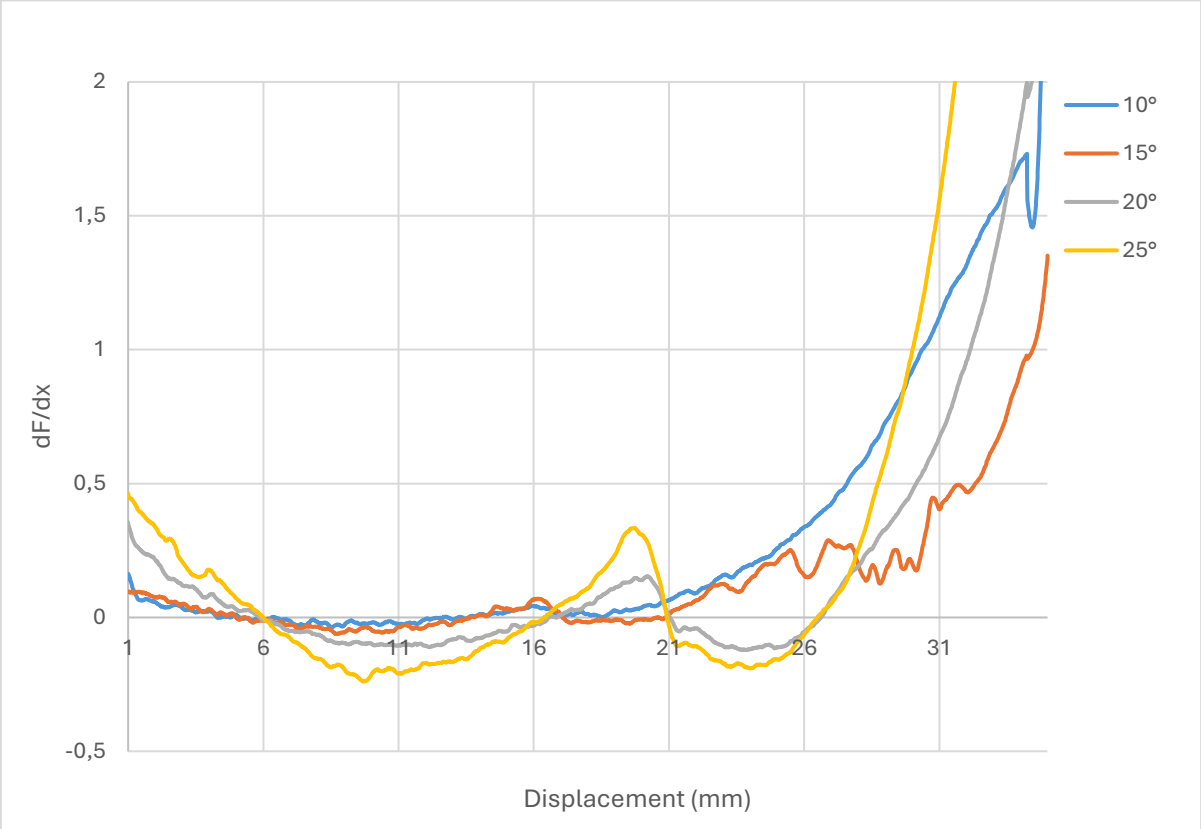


Figure 37. *Instantaneous stiffness (dF/dx) profiles as a function of displacement for 2×2 multi-cell matrices with varying cell angles (10°, 15°, 20° and, 25°).*

The curves of specimens with cell angles of 10° and 15° descend below the x-axis between ~6 mm and ~16 mm, forming a continuous valley. The curves of specimens with cell angles of 20° and especially 25° intersect the x-axis multiple times, creating a wavy form and two distinct deep valleys.

The first deep valley of the specimen with a 25° cell angle indicates a severe snap-through of the first row of cells. The sudden return of the curve above zero at ~20 mm is critical; this

indicates that the first row has finished deploying, the row has passed to other cells, and the structure has begun to carry load again instead of releasing energy. The second deep valley is the moment when the remaining cells overcome their own barriers. After ~26 mm, all rotating squares reach their geometric limits, and the mechanism locks. The cellular mechanism ends, and the material begins to behave like a monolithic structure, exhibiting high global stiffness.

The 22–35 mm displacement region (Figure 38) illustrates the final force behaviour in the monolithic tensile phase, where the cellular rotation mechanism ends and the structure locks.

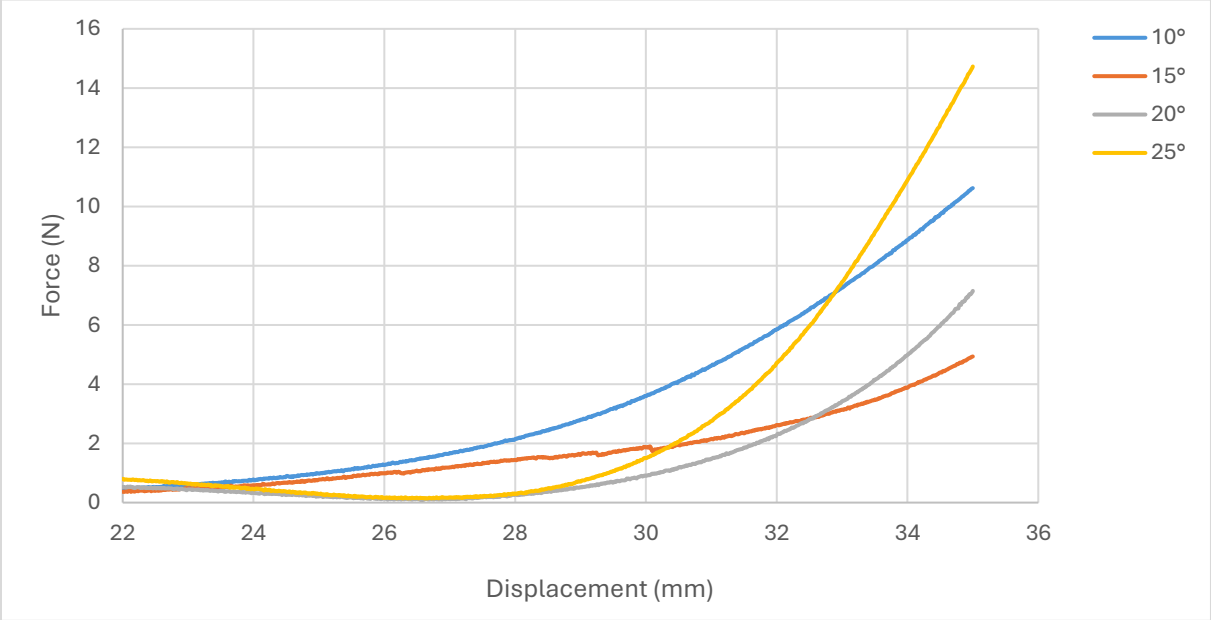


Figure 38. *Enlarged view of the force-displacement curves in the final deployment region (22-36 mm) for 2x2 specimens with varying cell angles.*

The specimen with a 25° cell angle, while shifting the onset of structural locking to a higher displacement, exhibiting a near-zero force plateau up to approximately 28 mm of displacement. It demonstrates the steepest slope when locking occurs. Reaching a force of approximately 14.5 N at 35 mm, it forms the most structurally resistant open form among the tested specimens.

The specimen with a 10° cell angle is the model that finishes its rotational movement at lowest displacement and begins to carry axial load at approximately 22 mm. After locking, it exhibits a linear slope, reaching ~10.5 N at 35 mm.

The specimen with 20° cell angle behaves similarly to the 25° model by delaying its locking phase until 28 mm; yet, its subsequent stiffness is lower. It reaches ~7 N at 35 mm.

The specimen with a 15° cell angle, although starting to lock early, is the configuration with the lowest slope by far. It can carry a load of ~5 N at a maximum displacement of 35 mm, which indicates that its ultimate rigidity in its open form is less compared to all other angles.

All critical parameters obtained from the kinematic and structural analyses are presented in Table 5 to summarize the effect of cell angle.

Table 5. *Summary of key mechanical properties for 2x2 specimens with varying cell angles.*

Cell Angle (°)	Initial Stiffness (N/mm)	1st Peak Force (N)	Displacement at Peak (mm)	Stiffness at 35 mm (N/mm)	Max Load at 35 mm (N)
10	0.07	~0.35	5	1.68	~10.5
15	0.11	~0.55	5	1.00	~5
20	0.48	~0.95	6	2.16	~7
25	0.49	~1.55	7	3.66	~14.5

4.2.3. 4 x 4 Specimens with Different Hinge Thicknesses

Scaling the unit cell topology from a 2x2 to a 4x4 matrix introduces complex multi-cell interactions and allows for the evaluation of macroscopic auxetic response. While the 2x2 matrix isolates the basic rotational mechanics, the 4x4 configuration, tested up to a maximum displacement of 70 mm, demonstrates how varying hinge thicknesses control global stiffness and sequential deployment.

In this analysis, all other parameters constituting the basic geometry of the structure were kept constant as control variables. The constant reference values are the same as with the 2x2 cells and are as follows:

- Side length of the rotating rigid squares: 30.0 mm

- Variation of the deviation of the cutting lines from the vertices: 3.0 mm

- Cell angle: 15°

- Hinge length: 3.75 mm

Three different hinge thicknesses were designed as independent variables: 0.8 mm, 1.2 mm, and 1.6 mm. 3D manufacturing of these three designs was completed using optimized parameters, and the samples were subjected to uniaxial tensile testing under the standard conditions detailed earlier.

Following the completion of the tensile tests, simultaneous force-displacement data obtained from the device were compiled and a comparative analysis was presented. This data quantitatively reveals the effect of hinge thickness, chosen as an independent variable, on the bistable behaviour and global stiffness of the structure. Figure 39 shows the initial configuration of the sample with a 4x4 matrix in the tensile testing machine.

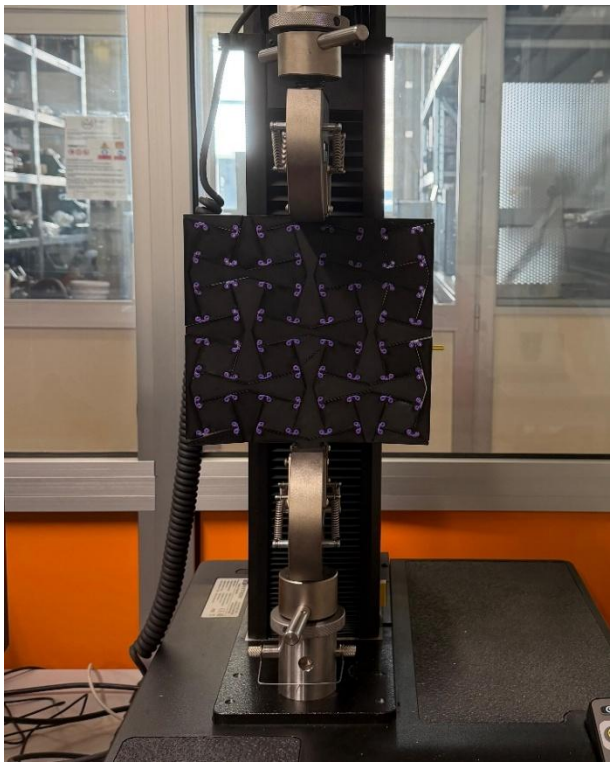


Figure 39. *The initial configuration of the 4x4 multi-cell specimen mounted in the universal testing machine.*

In Figure 40, the tensile test results of three different configurations of a 4x4 multicell matrix structure and hinge thicknesses of 0.8 mm, 1.2 mm and 1.6 mm are presented on a single graph.

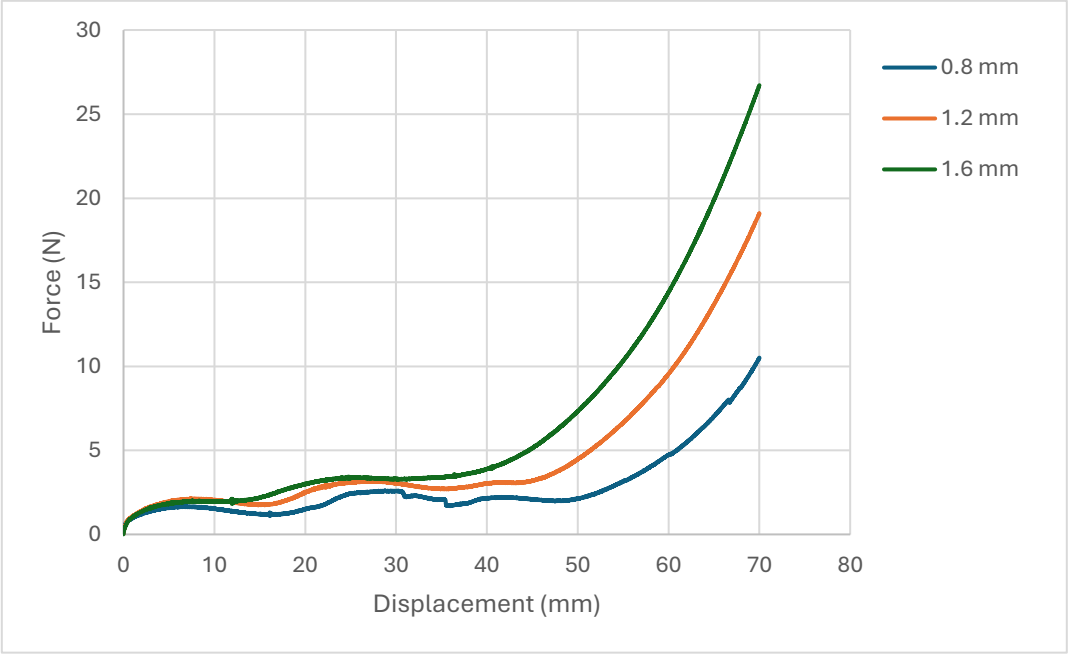


Figure 40. *Force-displacement curves of 4x4 specimens*

The enlarged force-displacement curves (figure 41) detail the initial kinematic response of 4x4 multi-cell structures with varying hinge thicknesses. This shows the initial macroscopic energy barrier and activation phase of the 4x4 matrix structure.

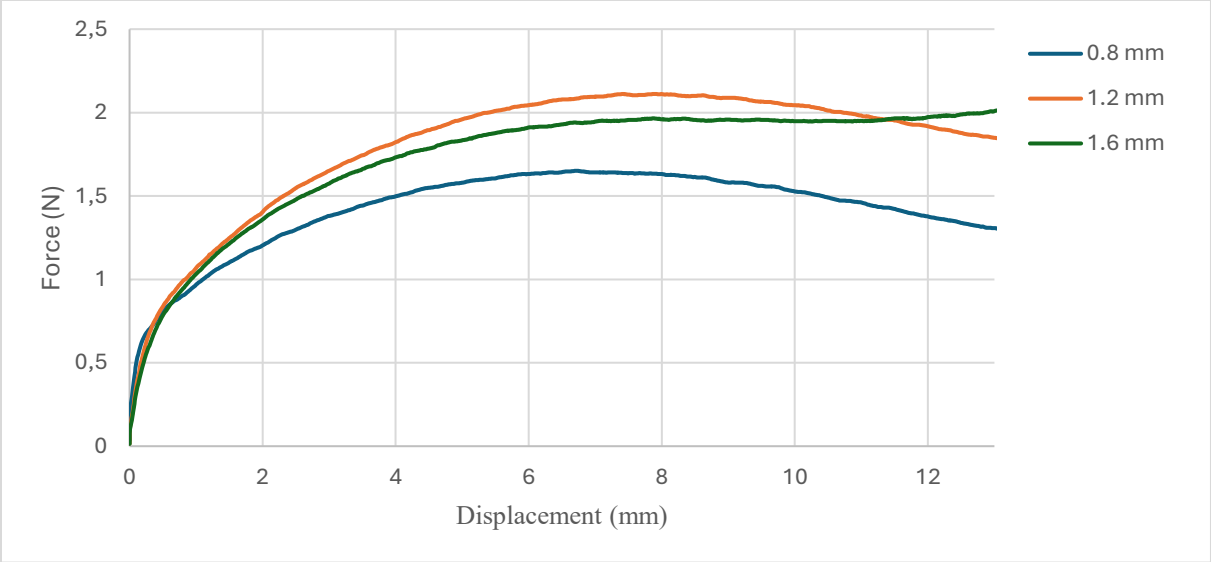


Figure 41. *Enlarged view of the force-displacement curves in the initial displacement region (0-13 mm) for 4x4 specimens with varying hinge thicknesses.*

In the initial 0-2 mm displacement range, the 0.8 mm thick specimen exhibits the lowest slope and gives the lowest initial stiffness value 0.26. As the hinge thickness increases, the initial resistance to rotation of the system increases significantly; therefore, specimens with other hinge thicknesses are estimated to have higher initial stiffness values. 0.36 was estimated for 1.2 mm and 0.42 for 1.6 mm.

A 0.8 mm sample reaches its first peak force of approximately 1.65 N at a displacement of about 6.5 mm. After this point, the curve begins to bend downwards, indicating that the first cell row has overcome the energy barrier and undergone a snap-through response, exhibiting bistable-like behaviour.

The 1.2 mm specimen shows that with increasing thickness, the peak shifts to both a higher force (~2.1 N) and a greater displacement (~7.5 mm). This indicates that the thick hinged matrix demands significantly more elastic energy to trigger the initial rotation.

The curve of the specimen with a 1.6 mm thick hinge reaches a value of approximately 2.0 N in ~7.5 mm. Unlike the other specimens, the absence of significant negative stiffness suggests that the high shape strain energy suppresses the occurrence of negative stiffness, and the mechanism resists with a high restoring force before completing the rotation.

In the subsequent displacement range of 10–40 mm (figure 42), the rigid PLA squares in the center rotate around the flexible TPU hinges, driving the macroscopic deployment and creating a negative Poisson's ratio. Unlike the 2x2 specimens, which deploy almost simultaneously, the 4x4 matrix exhibits force fluctuations in this range. Each fluctuation in the force-displacement curve corresponds to the sequential rotational movement of the individual square cells from top to bottom, guided by the lower grip held stationary during the upward pull movement. The gradual, rather than simultaneous, deployment of the cells in the macroscopic

matrix creates this fluctuating profile in the graph. Each increase in force indicates that a new row of cells has met the load, while each negative stiffness indicates that that row has completed its rotational movement and reached its deployed state.

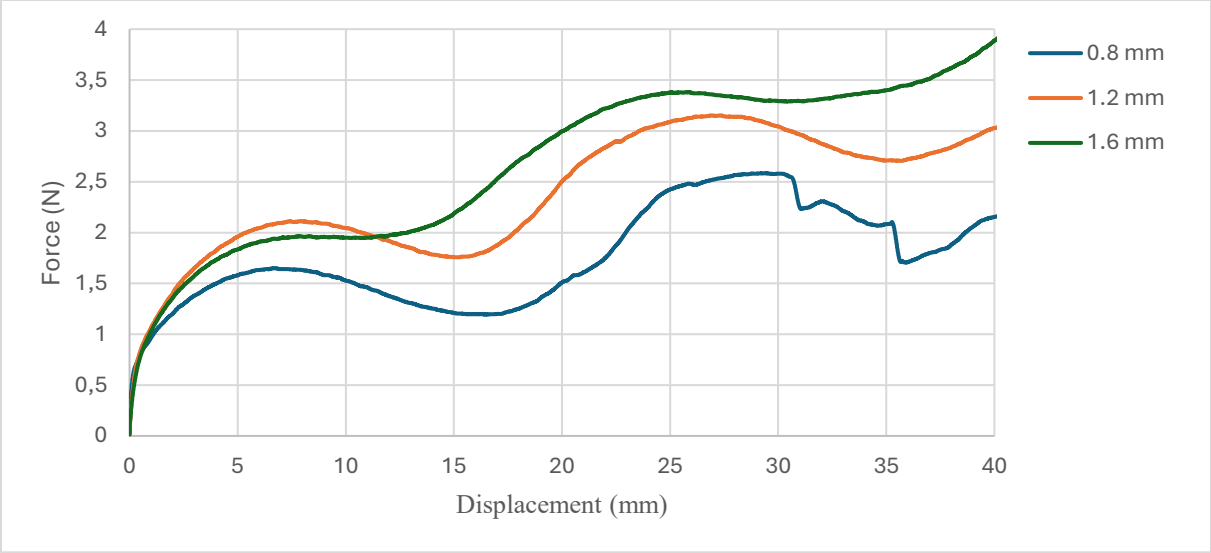


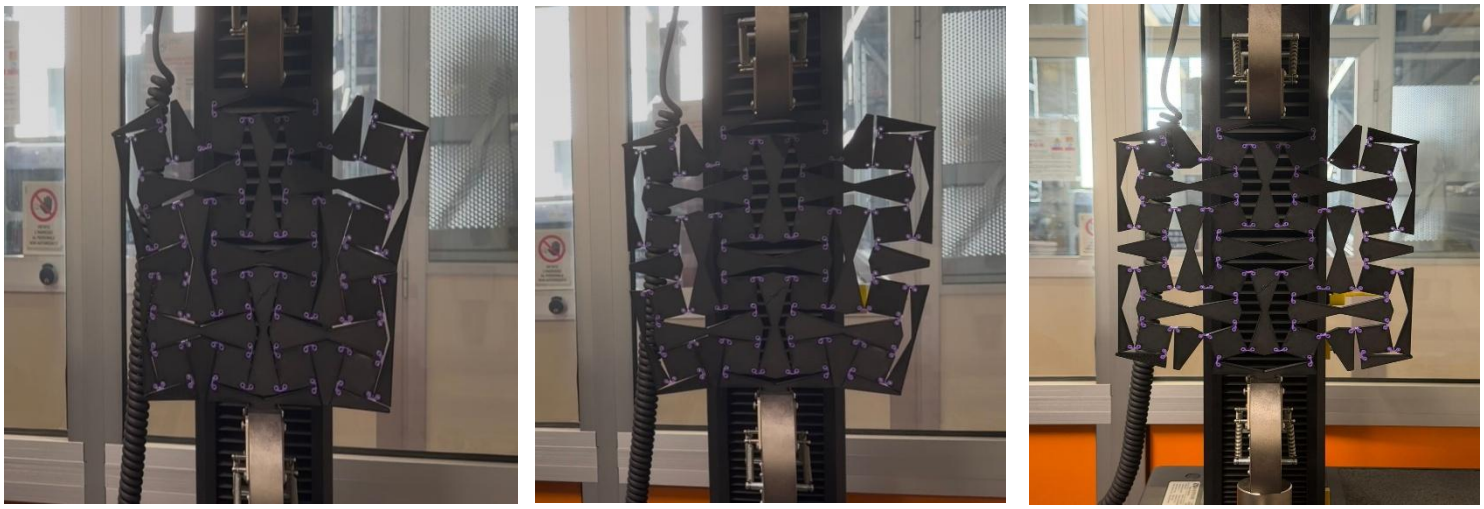
***Figure 42**. Force-displacement curves of the 4x4 matrix in the 0–40 mm displacement range for specimens with varying hinge thicknesses.*

The force drops above the 0.8 mm sample curve are sharp and deep. This confirms that thin hinges cannot generate the restoring energy to overcome the structural lock and exhibit a bistable-like behaviour.

In the 1.2 mm sample, it is observed that the force drops turn into a softer fluctuating profile instead of sharp drops. As the hinge thickness increased, the bistable-like behaviour of the system weakened.

In the sample curve containing a 1.6 mm thick hinge, the pronounced valleys and force drops have almost completely disappeared. The high strain energy stored in the thick hinge prevents the system from being retained in the deployed state, indicating that the macroscopic structure exhibits a monostable tendency with a high restoring force.

The visual sequence presented in Figure 43 directly confirms the multiple force fluctuations observed in the macroscopic force-displacement curves.



(a) *(b)* *(c)*

***Figure 43**. Visual sequence of the 4x4 matrix during tensile testing: (a) initial local opening at the top row, (b) progressive downward deformation of the middle rows, and (c) the fully deployed and structurally locked configuration.*

The rotational kinematics begins with a local opening corresponding to the first large peak force and subsequent abrupt drop, starting from the top row of the matrix (Figure 43-a). The lower grip remains fixed during the upward pull movement.

Figure 43-b illustrates this downward, gradual effect. As the upper row approaches its rotation limit, the middle rows are forced to activate and rotate. The activation of each row creates a distinct peak in the force profile in the macroscopic curve, physically demonstrating that auxetic expansion in scaled matrices occurs as a sequential chain reaction rather than a simultaneous global motion.

Consequently, Figure 43-c shows the fully deployed configuration. At this maximum displacement stage, all rotating rigid units have reached their geometric limits and are structurally locked. The cellular rotation mechanism is completely exhausted, and the multicellular matrix transforms into a single rigid body; this explains the sharp increase in stiffness after final deployment.

The instantaneous derivative at each point was calculated by determining the slope of the force-displacement curve. Since these derivative values represent stiffness, instantaneous stiffness curves were generated (dF/dx). To quantitatively evaluate the snap-through mechanics, the instantaneous stiffness (dF/dx) of the structures was derived from the smoothed force-displacement data. Figure 44 presents the instantaneous stiffness profiles for 4x4 specimens.

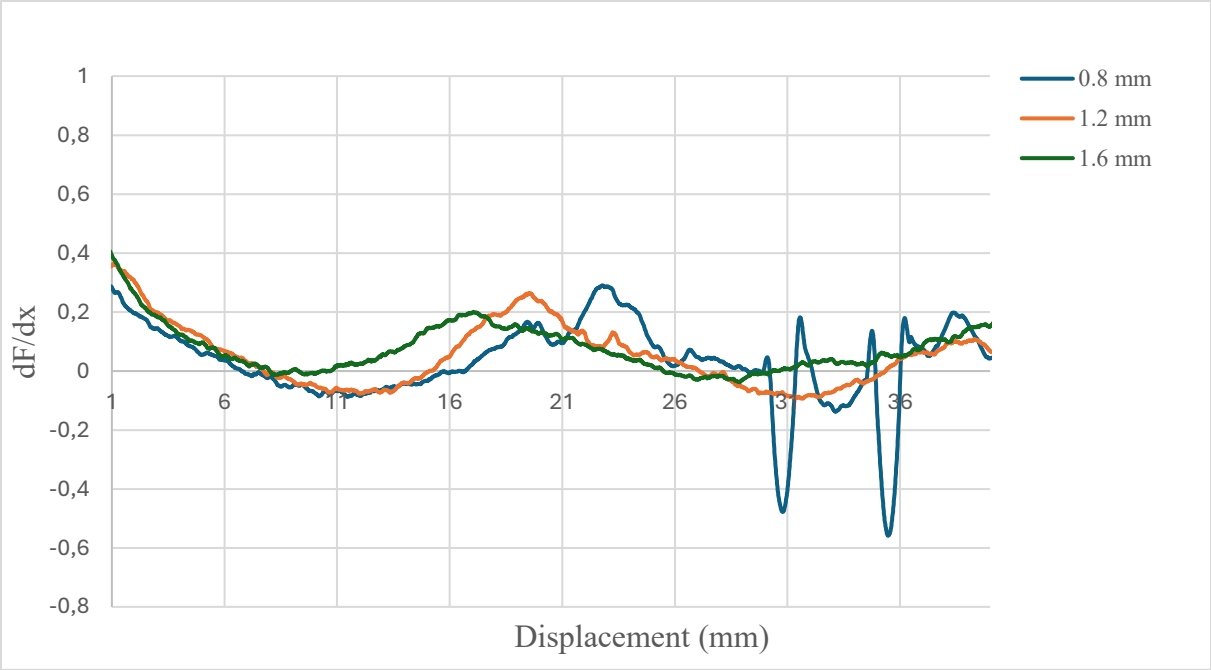


Figure 44. *Instantaneous stiffness (dF/dx) profiles as a function of displacement for 4x4 multi-cell matrices with varying hinge thicknesses (0.8 mm, 1.2 mm, and 1.6 mm)*

In the Force-Displacement curve, the specimen with a 0.8 mm hinge reaches its first peak around ~6.5 mm and then experiences a significant drop. In the derivative graph, at the onset of this force drop, it crosses the x-axis downwards, entering the "Negative Stiffness" region. This mathematically demonstrates that the first row of square cells in the matrix successfully snap-through by overcoming the energy barrier.

The point around ~11 mm is of critical importance, marking where the derivative curves for the 0.8 mm and 1.2 mm hinge samples reach their local minimum below zero. Mathematically, this point of maximum negative stiffness corresponds to the steepest downward slope in the force-displacement graph. Physically, it indicates that the first row of cells has overcome the energy barrier and is rapidly transitioning to the deployed state. During this snap-through phase, the structure autonomously releases energy rather than resisting the testing machine, thereby relieving the applied load and causing the steep force drop. The ~11 mm mark is the central point where this kinematic instability is most intense. In contrast, the derivative profile of the 1.6 mm thick hinge merely fluctuates around the zero line at this exact displacement. This mathematically reflects a plateauing force behaviour, proving that the thick hinges effectively resist the snap-through mechanism by storing higher elastic strain energy instead of buckling.

Examining the force-displacement curve in the 15-40 mm region reveals the characteristic sequential kinematic response of the 4x4 matrix. The 0.8 mm specimen exhibits sharp and deep force drops around the 30 mm and 36 mm displacements. In the derivative graph, these points correspond to significant negative stiffness troughs reaching -0.4 and -0.6. These deep troughs mathematically demonstrate that following the top row, the middle and bottom cell rows sequentially overcome their elastic energy barriers, resulting in a layer-by-layer deployment. During the deployment of these subsequent rows, the 1.2 mm hinge specimen displays mild oscillations just below the zero axis. Conversely, the derivative profile of the thickest 1.6 mm specimen remains predominantly positive throughout the 15-40 mm range.

This confirms that the high strain energy stored within the thick hinges suppresses the snap-through mechanism during the sequential deformation of the matrix, enforcing a globally monostable kinematic behaviour. Figure 45 illustrates the final force behaviour in the monolithic tensile phase, where the cellular rotation mechanism ends and the structure locks.

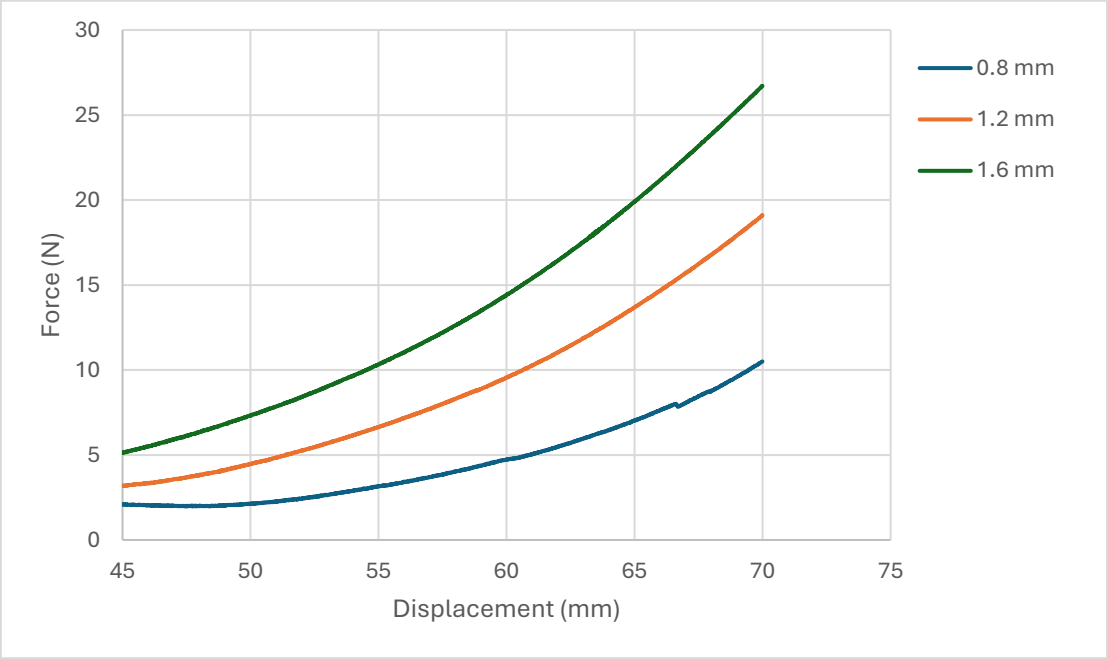


Figure 45. *Enlarged view of the force-displacement curves in the final deployment region (45-70 mm) for 4x4 specimens with varying hinge thicknesses.*

When the displacement reaches 50 mm, the rotating units reach their geometric limits and lock. From this point onwards, the mechanism behaves like a continuously rigid body, causing an increase in stiffness. At a maximum displacement of 70 mm, it is observed that the global stiffness is highly dependent on the hinge thickness.

When a 70 mm displacement is reached, the 0.8 mm thick sample remains at approximately 11 N, while the 1.2 mm sample reaches ~18 N, and the 1.6 mm thick sample reaches approximately 27 N load-carrying capacity. This supports the finding that increasing the thickness directly increases the global stiffness. It is also proven that increasing the number of cells leads to an increase in the global stiffness of the structure.

Linear fits were applied to estimate the final stiffness of the samples. Final stiffnesses were estimated as 0.80, 1.08, and 1.36 for samples with hinge thicknesses of 0.8, 1.2, and 1.6 mm, respectively. It was observed that the sample with thicker hinges exhibited higher stiffness at fully deployed states. The significantly higher calculated final stiffness value in this region numerically demonstrates how much stronger the structural integrity of the deployed structure is compared to thinner hinges.

All critical parameters obtained from the kinematic and structural analyses are presented in Table 6 to summarize the effect of hinge thickness.

Table 6. *Summary of key mechanical properties for 4x4 specimens with varying hinge thicknesses.*

Hinge Thickness (mm)	Initial Stiffness (N/mm)	1st Peak Force (N)	Displacement at Peak (mm)	Stiffness at 35 mm (N/mm)	Max Load at 70 mm (N)
0.8	0.26	~1.65	~6.5	0.80	~11.0
1.2	0.36	~2.10	~7.5	1.08	~18.0
1.6	0.42	~2.00	~7.5	1.36	~27.0

4.3. Considerations on Geometric Parameters and Cell Sizes

4.3.1. The Effect of Hinge Thickness

As seen in the test results, structures with thinner hinges successfully overcome the elastic energy barrier by performing the snap-through mechanism more easily and settle into a secondary stable energy well. When the instantaneous stiffness (dF/dx) profiles are examined, it is observed that the 0.8 mm samples undergo a significant transition to the negative stiffness regime and form a continuous local minimum. When the hinge thickness is increased to 1.6 mm, the high strain energy stored within the structure makes the snap-through movement difficult. The near disappearance of the negative stiffness region in the instantaneous stiffness graph (dF/dx) and the fact that the curve generally remains positive mathematically proves that the structure is forced into monostable kinematics. As the thickness increases, the global rigidity of the structure in both fully deployed and locked forms increases significantly. For example, in 2x2 matrices, a 0.8 mm specimen carries approximately 5 N of load at a maximum displacement of 35 mm, while a 1.6 mm specimen reaches approximately 16 N. In 4x4 matrices, this difference was measured as approximately 27 N compared to approximately 11 N at a displacement of 70 mm.

4.3.2. The Effect of Cell Angle

Based on the results, it can be stated that cell angle not only changes the static shape of the system but is also a critical kinematic parameter that determines the dynamic load-carrying capacity and opening behaviour of the structure. When the cell angle is kept small, such as 10° and 15°, the rotating rigid squares in the center are positioned very close together, and the voids within the system remain to a minimum. This causes the axial tensile force to be transmitted to all cells instantaneously, the cells to deploy almost simultaneously, and the initial peak force to remain low. When the cell angle is increased to 25°, the cut-off lines converge towards the center, and the inner squares become smaller, increasing the void tolerance in the system. These increased voids prevent the force from spreading instantaneously across the entire matrix and the cells overcome their barriers sequentially in groups. The fluctuating trend and two distinct deep valleys seen in the dF/dx graph of the 25° sample confirm this sequential snap-through movement. The 10° specimen completes its rotational movement much earlier, beginning to carry axial load at approximately 22 mm displacement, while the 25° specimen delays geometric locking to 28 mm. However, once locking occurs, the 25° specimen exhibits the steepest inclination, forming the stiffest open form with a load capacity of ~14.5 N.

4.3.3. The Effect of Matrix Size

While 2x2 matrices isolate the fundamental rotational mechanics and deploy almost simultaneously, 4x4 matrices exhibit sequential deployment. The fluctuations observed in the force-displacement curve in the range of 10-40 mm result from the progressive rotational deployment of cells in the macroscopic matrix from top to bottom. Each increase in force in the 4x4 matrix indicates that a new row of cells is resisting the applied load, while each negative stiffness response shows that the row has completed its rotational movement and is in the fully deployed state. These experimental findings physically demonstrate that auxetic expansion in scaled matrices is a sequential deployment process. Increasing the number of cells also increases the global stiffness of the structure.

5. Conclusions and Future Developments

In this study, rotating rigid unit models of auxetic materials, which have the potential to offer an innovative solution in aerospace applications were prototyped and characterized. The models were designed using the CAD software Altair Inspire and fabricated using the FDM/FFF method. Tough PLA, with its high elastic modulus and yield strength, was chosen for the rigid units in the model, while TPU 95A material with its high elongation at break was selected for the flexible hinges.

Parametric investigations revealed that by adjusting the hinge thickness (0.8, 1.2, 1.6 mm), cell angle (10°, 15°, 20°, 25°) and, cell matrix size (2x2, 4x4), the energy barrier, initial peak force, and global stiffness of the deployed structure could be controlled. It was observed that increasing the hinge thickness and cell angle generally increased the deployment force and deployment displacement. In addition, samples with thicker hinges stored higher elastic strain energy, which weakened the bistable-like behaviour of the mechanism. Variations in the matrix size of the cells provide critical information about force distribution. 2x2 matrices exhibited simultaneous deployment, while 4x4 configurations displayed sequential deployment behaviour. In addition, all modeled samples successfully exhibited auxetic behaviour by displaying a negative Poisson's ratio during testing.

Critical unloading tests, which would verify the true reversible bistability of the structures, were not performed; analyses are based on monotonic tensile tests. Since only one sample was tested for each configuration, statistical reliability regarding FDM-specific manufacturing deviations remains limited. Due to the viscoelastic nature of TPU material, the calculated stiffness and peak force values are instantaneous dynamic responses dependent on the applied strain rate and time-dependent stress relaxation.

Determining the most promising configuration directly depends on the requirements of the intended space mission. For a design with high stiffness and low strain energy, a high cell angle and thin hinge selection are ideal. In scenarios with limited power capacity, narrower angle designs are ideal to reduce the initial energy barrier required for deployment. If the mission requires maximum resistance and load-carrying capacity when the structure is fully deployed, thicker hinge designs are ideal. However, the increased strain energy with increasing hinge thickness should not be ignored. Because this weakens the bistable-like behaviour.

The selection of the final design requires careful engineering optimization to balance deployment energy, structural rigidity, and the required degree of bistable stability. In the future, work will focus on conducting cyclic tests to evaluate fatigue behaviour, developing FEA models, and testing these prototypes under simulated space conditions.

6. References

1) Litteken, D.A., 2019, March. Inflatable technology: using flexible materials to make large structures. In *Electroactive polymer actuators and devices (EAPAD) XXI* (Vol. 10966, p. 1096603). SPIE.
2) Pellegrino, Sergio. "Deployable structures in engineering." In *Deployable structures*, pp. 1-35. Vienna: Springer Vienna, 2001.
3) Kiper, G. and Soylemez, E., 2009, June. Deployable space structures. In *2009 4th International conference on recent advances in space technologies* (pp. 131-138). IEEE.
4) Pellegrino, S., 2001. Deployable structures in engineering. In *Deployable structures* (pp. 1-35). Vienna: Springer Vienna.
5) Wang, B., Zhu, J., Zhong, S., Liang, W. and Guan, C., 2024. Space deployable mechanics: A review of structures and smart driving. *Materials & Design*, *237*, p.112557.
6) Mobrem, M. and Spier, C., 2012, May. Design and performance of the telescopic tubular mast. In *Proceedings of the 41st Aerospace Mechanisms Symposium* (pp. 127-140). Washington DC: NASA
7) Gantes, C.J., Connor, J.J., Logcher, R.D. and Rosenfeld, Y., 1989. Structural analysis and design of deployable structures. *Computers & Structures*, *32*(3-4), pp.661-669.
8) Seo, S. and Han, M.W., 2025. A review on deployable structures in space industry. *International Journal of Precision Engineering and Manufacturing-Smart Technology*, *3*(1), pp.83-96.
9) ESA (2016) Large double pantograph reflector. [Online image] Available at: https://www.esa.int/ESA_Multimedia/Images/2016/11/Large_double_pantograph_reflector. [Accessed: Sep. 5, 2026].
10) Sultan, C. and Skelton, R., 2003. Deployment of tensegrity structures. *International Journal of Solids and Structures*, *40*(18), pp.4637-4657.
11) Kim, K., Chen, L.H., Cera, B., Daly, M., Zhu, E., Despois, J., Agogino, A.K., SunSpiral, V. and Agogino, A.M., 2016, October. Hopping and rolling locomotion with spherical tensegrity robots. In *2016 IEEE/RSJ international conference on intelligent robots and systems (IROS)* (pp. 4369-4376). IEEE
12) Puig, L., Barton, A. and Rando, N., 2010. A review on large deployable structures for astrophysics missions. *Acta astronautica*, *67*(1-2), pp.12-26.
13) Belvin, W.K., Straubel, M., Wilkie, W.K., Zander, M., Fernandez, J.M. and Hillebrandt, M., 2016. Advanced deployable structural systems for small satellites.
14) W Keith Belvin et al. “Advanced deployable structural systems for small satellites”. In: NATO CSO STO Specialist Meeting AVT-257/RSM-041 on Best Practices for Risk Reduction for Overall Space Systems. 2016.
15) Wang, B., Zhu, J., Zhong, S., Liang, W. and Guan, C., 2024. Space deployable mechanics: A review of structures and smart driving. *Materials & Design*, *237*, p.112557.

16) Kamaliya, P.K. and Upadhyay, S.H., 2023. Inflatable antenna structures: Deployment analysis of torus bounded Z-fold scalable planar membrane reflector. *Thin-Walled Structures*, *191*, p.111061.
17) NASA (2016) BEAM expansion progress. [Online image] Available at: https://www.planetary.org/space-images/beam-expansion-progress
18) Mendhe, S.E. and Kosta, Y.P., 2011. Metamaterial properties and applications. *International Journal of Information Technology and Knowledge Management*, *4*(1), pp.85-89.
19) Greaves, G.N., Greer, A.L., Lakes, R.S. and Rouxel, T., 2011. Poisson's ratio and modern materials. *Nature materials*, *10*(11), pp.823-837.
20) Chen, F., Wang, X.B., Du, Y.H. and Tang, C.A., 2022. Numerical experiment research on failure characteristics of anchored rock with negative Poisson's ratio bolt. *Frontiers in Earth Science*, *10*, p.899755.
21) Alderson, A. and Alderson, K.L., 2007. Auxetic materials. *Proceedings of the Institution of Mechanical Engineers, Part G: Journal of Aerospace Engineering*, *221*(4), pp.565-575.
22) Evans, K.E., Nkansah, M.A., Hutchinson, I.J. and Rogers, S.C., 1991. Molecular network design. *Nature*, *353*(6340), pp.124-124.
23) Lakes, R., 1987. Foam structures with a negative Poisson's ratio. *Science*, *235*(4792), pp.1038-1040.
24) Frolich, L.M., LaBarbera, M. and Stevens, W.P., 1994. Poisson's ratio of a crossed fibre sheath: the skin of aquatic salamanders. *Journal of Zoology*, *232*(2), pp.231-252.
25) Williams, J.L. and Lewis, J.L., 1982. Properties and an anisotropic model of cancellous bone from the proximal tibial epiphysis.
26) Evans, K.E. and Alderson, A., 2000. Auxetic materials: functional materials and structures from lateral thinking!. *Advanced materials*, *12*(9), pp.617-628.
27) Kolken, H.M. and Zadpoor, A.A., 2017. Auxetic mechanical metamaterials. *RSC advances*, *7*(9), pp.5111-5129.
28) Gibson, L.J. and Ashby, M.F., 1982. The mechanics of three-dimensional cellular materials. *Proceedings of the Royal Society of London. Series A, Mathematical and Physical Sciences*, pp.43-59.
29) Evans, K.E., Nkansah, M.A., Hutchinson, I.J. and Rogers, S.C., 1991. Molecular network design. *Nature*, *353*(6340), pp.124-124.
30) Masters, I.G. and Evans, K.E., 1996. Models for the elastic deformation of honeycombs. *Composite structures*, *35*(4), pp.403-422.
31) Li, C., Ma, N., Deng, Q. and Han, Q., 2024. Deformation and energy absorption of the laminated reentrant honeycomb structures under static and dynamic loadings. *Mechanics of Advanced Materials and Structures*, *31*(11), pp.2472-2482.
32) Choudhry, N.K., Panda, B. and Dixit, U.S., 2023. Energy absorption characteristics of fused deposition modeling 3D printed auxetic re-entrant structures: a review. *Journal of Materials Engineering and Performance*, *32*(20), pp.8981-8999.
33) Mohamad Razali, N.F., Mohd Sahar, N., Islam, M.S., Alawad, M.A. and Islam, M.T., 2025. Recent developments of auxetic metamaterials. *Advances in Physics: X*, *10*(1), p.2548208.

34) UCLA LEMUR, (t.y.). *Designing auxetic structures from unit cells*.
35) Prall, D. and Lakes, R.S., 1997. Properties of a chiral honeycomb with a Poisson's ratio of—1. *International Journal of Mechanical Sciences*, *39*(3), pp.305-314.
36) Attard, D., Casha, A.R. and Grima, J.N., 2018. Filtration properties of auxetics with rotating rigid units. *Materials*, *11*(5), p.725.
37) Tao, Z., Ren, X., Sun, L., Zhang, Y., Jiang, W., Zhao, A.G. and Xie, Y.M., 2022. A novel re-entrant honeycomb metamaterial with tunable bandgap. *Smart Materials and Structures*, *31*(9), p.095024.
38) Kim, Y., Son, K.H. and Lee, J.W., 2021. Auxetic structures for tissue engineering scaffolds and biomedical devices. *Materials*, *14*(22), p.6821.
39) Wu, W., Hu, W., Qian, G., Liao, H., Xu, X. and Berto, F., 2019. Mechanical design and multifunctional applications of chiral mechanical metamaterials: A review. *Materials & design*, *180*, p.107950.
40) Hou, R., Dong, P., Hu, J., Gong, Z., Sadeghzade, S., Cao, J. and Yuan, H., 2024. An optimized lozenge-chiral auxetic metamaterial with tunable auxeticity and stiffness. *Materials & Design*, *237*, p.112530.
41) Grima, J.N. and Evans, K.E., 2000. Auxetic behavior from rotating squares. *Journal of materials science letters*, *19*(17), pp.1563-1565.
42) Zhang, Z., Tian, Z., Mei, Y. and Di, Z., 2021. Shaping and structuring 2D materials via kirigami and origami. *Materials Science and Engineering: R: Reports*, *145*, p.100621.
43) van Manen, T., Janbaz, S., Ganjian, M. and Zadpoor, A.A., 2020. Kirigami-enabled self-folding origami. *Materials Today*, *32*, pp.59-67.
44) Xu, R., Chen, C., Sun, J., He, Y., Li, X., Lu, M.H. and Chen, Y., 2023. The design, manufacture and application of multistable mechanical metamaterials-a state-of-the-art review. *International Journal of Extreme Manufacturing*, *5*(4), p.042013.
45) Liu, T. and Hao, G., 2022. Design of deployable structures by using bistable compliant mechanisms. *Micromachines*, *13*(5), p.651.
46) Sansusthy Tardio, E., 2025. *Modeling and Characterization of Bistable Materials: Rotating Auxetic Surfaces and Shape Memory Alloys* (Doctoral dissertation).
47) Zhang, B., Meng, Z. and Wang, Y., 2025. 3D auxetic metamaterials with tunable multistable mechanical properties. *Mechanics of Materials*, *201*, p.105217.
48) Rafsanjani, A. and Pasini, D., 2016. Bistable auxetic mechanical metamaterials inspired by ancient geometric motifs. *Extreme Mechanics Letters*, *9*, pp.291-296.
49) Shang, X., Liu, L., Rafsanjani, A. and Pasini, D., 2018. Durable bistable auxetics made of rigid solids. *Journal of Materials Research*, *33*(3), pp.300-308.
50) Silverberg, J.L., Na, J.H., Evans, A.A., Liu, B., Hull, T.C., Santangelo, C.D., Lang, R.J., Hayward, R.C. and Cohen, I., 2015. Origami structures with a critical transition to bistability arising from hidden degrees of freedom. *Nature materials*, *14*(4), pp.389-393.
51) Bangert, M., 2021. Additive manufacturing standards. *Quality*, *60*(5), pp.60-62.
52) Dizon, J.R.C., Espera Jr, A.H., Chen, Q. and Advincula, R.C., 2018. Mechanical characterization of 3D-printed polymers. *Additive manufacturing*, *20*, pp.44-67.

53) Dubey, D., Singh, S.P. and Behera, B.K., 2025. Mechanical, thermal, and microstructural analysis of 3D printed short carbon fiber-reinforced nylon composites across diverse infill patterns. Progress in Additive Manufacturing, 10(2), pp.1671-1689.
54) Gonabadi, H., Yadav, A. and Bull, S.J., 2020. The effect of processing parameters on the mechanical characteristics of PLA produced by a 3D FFF printer. *The International Journal of Advanced Manufacturing Technology*, *111*(3), pp.695-709.
55) Kristiawan, R.B., Imaduddin, F., Ariawan, D., Ubaidillah and Arifin, Z., 2021. A review on the fused deposition modeling (FDM) 3D printing: Filament processing, materials, and printing parameters. *Open Engineering*, *11*(1), pp.639-649.
56) Aumnate, C., Pongwisuthiruchte, A., Pattananuwat, P. and Potiyaraj, P., 2018. Fabrication of ABS/graphene oxide composite filament for fused filament fabrication (FFF) 3D printing. *Advances in Materials Science and engineering*, *2018*(1), p.2830437.
57) Mizzi, L., Salvati, E., Spaggiari, A., Tan, J.C. and Korsunsky, A.M., 2020. Highly stretchable two-dimensional auxetic metamaterial sheets fabricated via direct-laser cutting. *International Journal of Mechanical Sciences*, *167*, p.105242.
58) Chen, X.Y., Underhill, R.S. and Rodrigue, D., 2023. A simple method to convert cellular polymers into auxetic metamaterials. *Applied Sciences*, *13*(2), p.1148.